ELEMENTA
Science of the Anthropocene

RESEARCH ARTICLE

Atmospheric forcing and photo-acclimation of phytoplankton fall blooms in Hudson Bay

Lucas Barbedo[1,2,*], Simon Bélanger[1,*], Jennifer V. Lukovich[3], Paul G. Myers[4], and Jean-Éric Tremblay[5]

Pulses of ocean primary productivity during the fall season are frequent in the mid-latitudes when ocean cooling and wind-driven turbulence erode the surface stratification and allow the injection of nutrients into the euphotic zone. This phenomenon is often referred to as a phytoplankton fall bloom, and can play an essential role in the survival of marine species during winter. In Hudson Bay, we found that pelagic fall blooms are triggered when the convective mixing, forced mainly by atmospheric cooling and to a lesser extent to wind-driven turbulence, expands the mixed layer, ventilates the pycnocline, and likely erodes the nitracline. Ocean color observations were used to assess the seasonal variability of phytoplankton photo-acclimation state from the ratio of phytoplankton carbon (C_{phy}) to chlorophyll-*a* concentration ([*chla*]). C_{phy} was estimated using the satellite-derived particulate backscattering coefficient (b_{bp}) after subtraction of the non-algal backscattering background. We found a systematic increase in C_{phy} and C_{phy}:[*chla*] from mid-summer to fall season indicating that fall blooms are potentially productive in term of organic carbon fixation.

1. Introduction

In polar seas, ongoing climatic changes have subjected phytoplankton dynamics to a new configuration of physical forcings that control incoming light, nutrient availability, and water column structure, with impacts on all marine trophic levels (Leu et al., 2011; Wassmann, 2011; Ardyna et al., 2014). Nowadays, sea-ice retreat is occurring earlier and recovering later (Markus et al., 2009; Stroeve et al., 2011; Stroeve et al., 2014), lengthening the open water season (Arrigo and van Dijken, 2015). Consequently, annual phytoplankton production rises because more light is available in the upper ocean layer (Bélanger et al., 2013; Arrigo and van Dijken, 2015). In turn,

phytoplankton phenology, i.e., the seasonal succession of phytoplankton processes, impacts the carbon pump, pelagic ecosystems, the benthic realm, and valuable fish stocks (Platt et al., 2003; Friedland et al., 2008; Barber et al., 2015). The synchronization between phytoplankton bloom timing and organisms in early life and sensitive developmental stages (eggs or larval) is essential for species survival and recruitment (match/mismatch hypothesis: Cushing, 1990). Satellite observations have suggested that fall bloom occurrence has risen in high northern latitudes during the last decades (Ardyna et al., 2014). In low productive ecosystems like Hudson Bay (Tremblay et al., 2019), the world's most extensive inland sea, an increase of phytoplankton abundance in the fall season can supply extra energy stock for polar species, increasing their overwintering potential.

Field and satellite observations in the middle- and high-northern latitudes have confirmed the importance of fall blooms. For instance, Rho and Whitledge (2007) showed that sediment traps recorded a high flux of organic carbon during the summer–fall transition in the Bering Sea. Sigler et al. (2014) reported that large crustacean zooplankton taxa respond to interannual variability in the time interval between spring and fall blooms in the Eastern Bering Sea. In general, short-term physical events, like storms, are assumed to affect the dynamics of fall blooms, as observed over the Nova Scotia Shelf (Greenan et al., 2004) and the sub-polar Japan/East Sea (Kim et al., 2007). Strength of wind-fetch and sea surface freezing

[1] Département de biologie, chimie et géographie, Groupes BORÉAS et Québec-Océan, Université du Québec à Rimouski, Rimouski, QC, Canada

[2] Current affiliation: Stennis Space Center, School of Ocean Science and Engineering, Division of Marine Science, The University of Southern Mississippi, MS, USA

[3] Center for Earth Observation Science, Department of Environment and Geography, University of Manitoba, Winnipeg, MB, Canada

[4] Department of Earth and Atmospheric Sciences, University of Alberta, Edmonton, AB, Canada

[5] Takuvik Joint International Laboratory, Département de biologie et Québec-Océan, Laval University, Québec City, QC, Canada

* Corresponding author:
Email: lucasbarbedo@gmail.com; simon_belanger@uqar.ca

delays have intensified phytoplankton blooms triggered by the transport of nutrients into the euphotic zone, as reported by Rho and Whitledge (2007) in the Bering Sea shelf, Fujiwara et al. (2018) in the Chukchi Sea, and Ardyna et al. (2014) and Castro de la Guardia et al. (2019) in the Arctic Ocean. Although recent studies have sought to understand the dynamics of phytoplankton fall blooms, information is still lacking about processes that trigger and maintain the effective productivity of fall blooms in north polar seas.

The Hudson Bay System (HBS) drainage basin alone equates to 18% of the total freshwater input of the Arctic Ocean (Déry et al., 2005; Granskog et al., 2011), while melting sea ice supplies twice this freshwater volume during a short melting period throughout the spring-to-summer transition (Mysak et al., 1996). The stratification resulting from this large amount of freshwater produces persistent oligotrophy in the summer (Harvey et al., 1997; Ferland et al., 2011; Lapoussiere et al., 2013; Xi et al., 2013; Tremblay et al., 2019). Ferland et al. (2011) reported low primary production rates in late summer (August and early September) dominated by small-sized phytoplankton adapted to oligotrophic and stratified conditions. In contrast, Xi et al. (2013) measured higher chlorophyll-a concentration ($[chla]$) and phytoplankton absorption coefficient in the fall (end of September to early October) compared to summer (July), suggesting an increase in primary productivity later during the open water season in the HBS. Recently, a systematic analysis of satellite-derived $[chla]$ suggested that phytoplankton biomass systematically increases during the summer-to-fall transition (Barbedo et al., 2020), but the mechanisms explaining this phenomenon were not examined in detail.

Atmospheric forcing (convection- and wind-driven turbulence) trigger vertical mixing during the fall season, promoting the seeding of the upper-water layer with phytoplankton communities that developed at the subsurface chlorophyll maximum (SCM) during the summer and pumping nutrients in the euphotic zone. SCM phytoplankton is adapted to low light levels (photo-acclimation) with large cells having high intracellular $chla$ content (Behrenfeld et al., 2002; Westberry et al., 2008; Cullen, 2015; Halsey and Jones, 2015; Marañón, 2015). Phytoplankton communities with high intracellular $chla$ content in an environment of low photosynthetically active radiation (PAR) and excessive turbulence can be saturated quickly in terms of net carbon fixation (low maximum rate of photosynthesis, P_{max}; Huot et al., 2013) and can result in a satellite overestimation of primary production (Sathyendranath et al., 2020). To gain insights about physiological state of the fall bloom, we investigated how satellite-based approaches can help to address this question.

Phytoplankton community size structure and photo-physiological aspects (i.e., photo-acclimation and photoadaptation) are key aspects for a better understanding of pelagic ecosystems in terms of productivity, food web complexity, and the biological pump (Antoine et al., 2011; Brewin et al., 2014; Sathyendranath et al., 2020). Behrenfeld et al. (2005) used a satellite-derived particle backscattering coefficient (b_{bp}) as a proxy of

phytoplankton carbon content (C_{phy}) allowing an estimation of the ratio of phytoplankton carbon to chlorophyll-a ($C_{phy}:[chla]$), a proxy of phytoplankton photoacclimation (Behrenfeld et al., 2002). Devred et al. (2011) derived phytoplankton size classes using chlorophyll-specific spectral absorption coefficient in the Canadian east coast and northwest Atlantic. Brewin et al. (2012) examined the chlorophyll-specific backscattering coefficient in relation with small (< 20 μm) and large (> 20 μm) phytoplankton size classes. In contrast, in Arctic waters where phytoplankton is not always the dominant optical component, spectral variations in remote sensing reflectance arise mainly from differences in the bio-optical environment in which specific communities are found (Reynolds and Stramski, 2019). To understand the phytoplankton photoacclimation state and its seasonal evolution, satellite-derived $C_{phy}:[chla]$ was estimated with a method that considered the non-algal contribution to b_{bp} (Bellacicco et al., 2019).

Our study focuses on the physical mechanisms responsible for the fall bloom phenomenon as well as potential photo-physiological adaptations of phytoplankton to late summer/fall conditions. Specifically, the objectives were to i) understand the role of atmospheric forcings and water column structure on fall bloom dynamics, and ii) assess the physiological state of phytoplankton communities blooming in the fall season using satellite-derived optical proxies.

2. Materials and methods

To investigate the role of atmospheric and oceanographic processes in triggering and maintaining phytoplankton fall blooms, we employed in synergy the outputs of an ice-ocean dynamic model, climatic reanalysis, the satellite ocean color constellation, and in situ bio-optic and radiometry. We discuss the seasonality of atmospheric and oceanographic interplays, water column evolution, and their effects on phytoplankton dynamics in Hudson Bay. In Southern Hudson Bay, inter-annual and seasonal variability of freshwater input results in remarkable shifts on stratification drivers, i.e., salinity and temperature vertical gradients. To better understand the counterpart of atmospheric forcing on the water column and phytoplankton dynamics, we focused on South Hudson Bay where more pronounced ice-edge and fall blooms were observed ($[chla] > 2$ mg m^{-3}), and where riverine input can contribute to the upper-layer stratification during the melting season.

To enlighten phytoplankton dynamics in the fall season, we compared two decades (1998–2018) of ocean color satellite observations with bio-optical conditions collected in situ during a recent Canadian expedition throughout marginal ice zones during the spring-to-summer transition in Hudson Bay (2018), when phytoplankton is expected to bloom. Therefore, spring in situ observations can support the satellite ocean color observations to fill in the lack of information in fall. We analyzed in detail both satellite-derived $[chla]$ and b_{bp} to explore the potential role of photo-acclimation on phytoplankton and its productivity during the fall season.

2.1. Ice-ocean model and heat-flux calculations

Vertical profiles of potential temperature and salinity were modeled using version 3.4 of the Nucleus for European Models of the Ocean (NEMO) general circulation model. NEMO is a coupled ice-ocean dynamic model. The experiments used the Arctic and Northern Hemisphere Atlantic configuration run at 1/4° resolution (ANHA4) and 5-day averaged output. The vertical resolution was 50 unevenly spaced levels, with the majority of the resolution in the upper column to capture the mixed layer and thermocline processes. The model inputs for atmospheric fields are taken from the Canadian Meteorological Centre's Global Deterministic Prediction System Re-Forecasts (CGRF; Smith et al., 2014), and the coupled ocean-ice Coordinated Ocean Research Experiments (CORE) bulk formula was used to compute fluxes between the atmosphere and the ocean and to assimilate wind stress into the momentum equations (Large and Yeager, 2004; 2009). River runoff within HBS was provided by calibrated output from the HYdrological Predictions for the Environment (HYPE; Lind-ström et al., 2010; Andersson et al., 2015; Gelfan et al., 2017). This runoff dataset has not been integrated with observations but included the improvements to the model, such as a better representation of La Grande Riv-ière discharge and Nelson River regulated. Outside HBS, runoff was compiled by Dai and Trenberth (2002), with the addition of Greenland melt by Bamber et al. (2012). Further details on the model setup and evaluation can be found in Ridenour et al. (2019).

Heat fluxes (in W m^{-2}), i.e., the difference in short- and long-wave radiation, latent and sensible heat between the atmosphere and the ocean, were computed using the bulk formulas developed by Large and Yeager (2004; 2009). The calculations considered near-surface atmospheric state (wind, potential temperature, specific humidity, and density), and the ocean state (ocean surface current and temperature). Briefly, sea-surface currents and sea-surface temperature (SST) were calculated from NEMO-ANHA4 model simulations. Atmospheric potential temperature, humidity, wind (10 m), precipitation, short and long-wave radiation were obtained from CGRF, which is assumed suitable to parameterize physical processes of polar seas and has a finer spatial-temporal scale (i.e., 33 km daily) than other current available global reanalysis (Smith et al., 2014).

2.2. Satellite ocean color

Values for [chla] (in mg m^{-3}), the particle backscattering coefficient at 443 nm ($b_{bp}(443)$, in m^{-1}), and the diffuse attenuation coefficient at 490 nm ($k_d(490)$, in m^{-1}) were downloaded from the Globcolour Project (http://www.globcolour.info/). Globcolour Level-3 [chla] (European Space Agency, 2020) and $b_{bp}(443)$ were estimated using the semi-analytical algorithm of Garver-Siegel-Maritorenna (GSM: Garver and Siegel, 1997; Maritorena et al., 2002). We performed an in situ evaluation of the GSM algorithm to ensure the robustness of our choice of for [chla] (Figure S1). The value for $b_{bp}(555)$ was calculated from $b_{bp}(443)$ using a power law function with a spectral dependency of -1.0337 (Maritorena et al., 2002). The value for $k_d(490)$ was estimated using the quasi-analytical

algorithm of Lee et al. (2005). The Globcolour Level-3 (i.e., binned and mapped) merged products have temporal and spatial resolutions of 1 day and 4.63 km, respectively, and cover the period of 1998 to 2018. The merged products improve the spatial-temporal coverage, diminishing gaps due to cloud cover and sea ice (Maritorena et al., 2010). The binning methodology combines radiometry from ocean color if the sensors are available, which include the Sea Wide Field-of-view Sensor (SeaWiFS: 1998–2010), Moderate Resolution Imaging Spectroradiometer (MODIS: 2002–2018) aboard the Aqua satellite, Medium-Resolution Imaging Spectrometer (MERIS: 2002–2011), Visible Infrared Imaging Radiometer Suite (VIIRS: 2012–2018), and Ocean and Land Colour Instrument (OLCI: 2016–present). Coastal areas with depths shallower than 50 m were removed from analysis to avoid turbidity and bottom effect. Satellite data were restricted to complex water non-scatter dominated and case water-1 (Lee and Hu, 2006) to avoid the influence of non-algal particle backscattering on estimation of C_{phy}.

2.3. Time-series analysis

We evaluated the effect of atmospheric forcing on the water column structure and phytoplankton dynamics in spatial bin areas of 100 × 100 ocean color pixels (approximately 4 km) centered on 84°W 57°N in southern Hudson Bay. Time series of heat flux, wind speed, light level, and [chla] were combined with water column profiles. The first optical depth (z_{OC}: in m), the water column layer inside the ocean color satellites range, and the euphotic zone depth (z_{eu}: in m), defined as the depth at which PAR reduces to 1% of the incoming surface value, were estimated using $k_d(490)$, i.e., $z_{eu} = -4.5/k_d(490)$ and $z_{OC} = -1/k_d(490)$, respectively. For that, NEMO simulations were used to produce a high resolution, basin-scale hindcast of ocean vertical structure of potential temperature, salinity, stratification, and mixed layer depth. The mixed layer thickness was calculated based on sea water density (ρ), i.e., the depth of a threshold value of density ($\Delta\rho = 0.01\ kg\ m^{-3}$) from a near-surface value (de Boyer Montégut et al., 2004). Fluid stratification was quantified using the buoyancy frequency (N^2), known as the Brunt-Vaissala frequency, i.e., the frequency required to break up the stratification (Equation 1):

$$N^2 = -\frac{g}{\rho}\frac{\partial p}{\partial z}, \tag{1}$$

where g is the gravity, ρ is the density, p is the pressure, and z is depth. The heat-flux inversion, i.e., day of the year when atmosphere began to cool the ocean, was detected by the first day in which the heat-flux sign was negative between June and November.

To indicate the ice-edge zone, the sea-ice retreat, t_R, was defined as the day at which sea-ice concentration (SIC) is below 10% for at least 24 days (Barbedo et al., 2020). SIC was obtained from the National Snow and Ice Data Center (NSIDC), which is based on daily multichannel passive microwave radiometry sensors clustered using the Bootstrap algorithm at 25-km resolution (Comiso et al., 1997; Comiso, 2000).
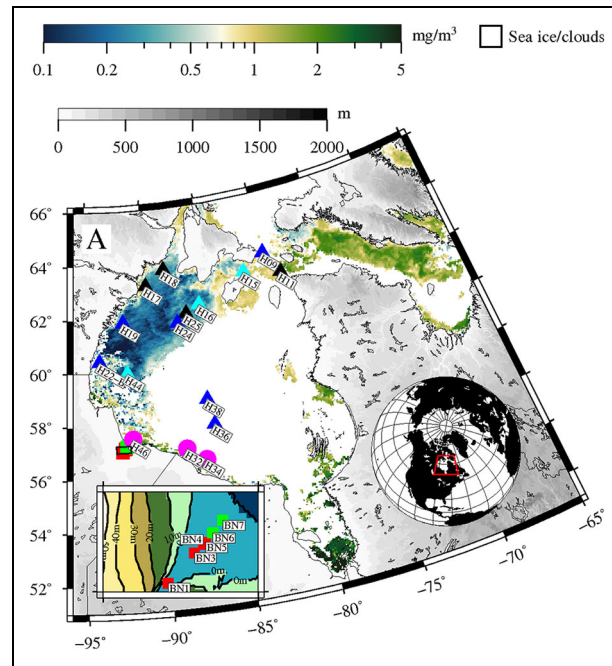
Figure 1. Bio-optical stations of the BaySys expedition, 2018. Distinct light environments sampled during the spring-to-summer transition in Hudson Bay. Represented are three light attenuation levels in the marginal-ice zone: high (cyan triangles), moderate (blue triangles), and low (black triangles); along with Nelson River sediment plume (red squares, inset); phytoplankton bloom under influence of Nelson River plume (green squares, inset); and landfast sea-ice load sediment in southern HB coastal waters (pink circles; Harasyn et al., 2019). Color maps were obtained from the Etopo continental topography (gray scale in meters above sea level; Amante and Eakins, 2009); monthly merged composition of chlorophyll-*a* concentration (color scale, in mg m^{-3}) for June 2018, obtained from the Globcolour Project.

2.4. In situ bio-optics

In situ bio-optical measurements were performed aboard the Canadian Icebreaker NCGC *Amundsen* during the BaySys expedition in Hudson Bay in June 2018 (Ahmed et al., 2021). The sampling was distributed over recently opened waters in western Hudson Bay in the marginal ice zone (MIZ), i.e., the area along the edge of the ice pack that is affected by open ocean processes (Barber et al., 2015), in leads surrounded by landfast ice loading/releasing sediment in the south, and along a transect in the Nelson River plume (**Figure 1**). The field measurements included in situ particle backscattering, pigment analysis and in-water radiometry, which are used to support our interpretation of the satellite-derived phytoplankton photoacclimation state described in the next section.

2.4.1. Backscattering coefficient

The total spectral backscattering coefficient, $b_b(\lambda)$, is the amount of light scattered by water molecules or suspended particles into the hemisphere from which light has originated. Total $b_b(\lambda)$ can be further divided in terms of additive components of pure water (b_{bw}) and particles (b_{bp}). The latter is a good proxy of particulate organic carbon (POC) in the open ocean (Stramski et al., 1999). Total $b_b(\lambda)$ was calculated from the volume scattering function (β: in sr^{-1}) measured at a fixed scattering angle (θ_b°) in the backward direction relative to the laser beam

using an ECO BB9 (Sea-Bird Scientific). The instrument was calibrated by the manufacturer before the field campaign. The BB9 operated at nine wavelengths (412, 440, 488, 510, 532, 595, 660, 675, and 715 nm) with $\beta(\theta_b^\circ = 117^\circ)$.

The measurements were performed at 14 stations in Hudson Bay. The data were processed using an open source R package (DOI: https://github.com/belasi01/Riops; see also Bélanger et al., 2017) following the manufacturer's protocol (Twardowski et al., 2007). Briefly, the spectral backscattering coefficient was obtained from the measured $\beta(\theta_b^\circ,\lambda)$ through integration over the backward hemisphere based on a phase function according to the Mie theory (wavelength-selective scattering) using the relation (Equation 2):

$$b_{bp}(\lambda) = 2\pi\chi_p\left[\beta(\theta_b^\circ,\lambda) - \beta_{sw}(\theta_b^\circ,\lambda)\right] \qquad (2)$$

where χ_p, a spectrally constant value of 1.1 (Boss and Pegau, 2001), represents the relationship between $\beta(\theta_b^\circ)$ and b_{bp}. The spectral contribution of pure seawater to scattering (β_{sw}) at θ_b° was computed using temperature and salinity at the same time and depth with a CTD sensor (Zhang et al., 2009). The dependence on absorption, a, caused by attenuation along with the sensor and light source path was corrected based on simultaneous measurements of total absorption by an absorption and attenuation spectral (ac-s: Sea-Bird Scientific) sensor according to recommendations of Doxaran et al. (2016). Profiles of $b_{bp}(\lambda,z)$ were binned at 0.1-m depth intervals after

applying a local polynomial regression smoothing function (Cleveland et al., 1992); $b_{bp}(555)$ was calculated at each depth by fitting a power law function to $b_{bp}(\lambda,z)$. Finally, b_{bp} at 555 nm was selected for further analysis because pigment absorption exhibits weak contribution in this spectral region, as reported by Reynolds et al. (2016).

2.4.2. Pigment analysis

Chlorophyll-*a* concentration from discrete samples were measured by the high-performance liquid chromatography (HPLC) technique ($[chla]_{HPLC}$: in mg m^{-3}). Seawater discrete samples of 1–3 L were collected using Niskin bottles and filtered onto Whatman GF/F filters (25 mm in diameter) under a gentle vacuum (3.98 Hg). The filters were placed immediately in 2-mL cryovials and flash-frozen in liquid nitrogen, then stored at −80°C until analysis. After the cruise, filters were extracted in 100% methanol at −20°C, disrupted by sonication, and clarified later by vacuum filtration through Whatman GF/F filters. Extraction time lasted 2 hours, and HPLC analysis was carried out the same day (Ras et al., 2008; Tran et al., 2013; Robinson et al., 2018). More details on the analytical methods can be found in Matthes et al. (2021) for the BaySys, and Ras et al. (2008) for the GreenEdge data sets. In this study, $[chla]_{HPLC}$ corresponds to the sum of *chla* and chlorophyllide-*a*.

2.4.3. In-water radiometry

Downwelling in-water irradiance profiles, $E_d(z,\lambda)$, were measured by Compact-Optical Profiling System (C-OPS; Hooker et al., 2013) built by Bio-Spherical Instruments Inc. (San Diego, California, USA). C-OPS has 19 bands distributed between the spectral range of 320 to 865 nm measuring the planar downwelling irradiance coupled with auxiliary sensors for water temperature, pressure, pitch and roll. A similar reference sensor in the ship deck measured above-water surface downwelling irradiance $E_d(0^+,\lambda)$. An above-water reference sensor was coupled to the Bioshade to measure the ratio of direct sun to diffuse sky irradiation (E_d^{sun}/E_d^{sky}; Morrow et al., 2010), which is used for instrument self-shadow correction.

We profiled at least three consecutive downcasts between the sea surface and a variable water depth corresponding to the approximate 1% light level. In-water radiometric measurements were normalized to account for the illumination variations during each cast. Underwater casts trespassing a vertical tilt of 5° were removed from the analysis. In-water radiometry was processed using the R-package COPS available in DOI: https://github.com/belasi01/Cops. A detailed discussion about the C-OPS instrument and the processing protocols can be found elsewhere (Mueller et al., 2003; Morrow et al., 2010; Antoine et al., 2013; Hooker et al., 2013; Bélanger et al., 2017).

The daily average of photosynthetic active radiation ($\overline{PAR}$) was computed after applying the factor $cos(\theta_s(t))/cos(\theta_{oncast})$, where θ_s is the solar zenith range in the daytime (t) and θ_{oncast} is the solar zenith on cast of the light profile (Reda and Andreas, 2004). *PAR* (in µmol

photons m^{-2}s^{-1}) was calculated from trapezoidal integration of $E_d(\lambda,z)$ in the visible spectrum from 400 to 700 nm (Equation 3):

$$PAR(z) = \frac{1}{\hbar c}\frac{1}{N}\int_{\lambda=400}^{700nm}\lambda E_d(\lambda,z)\,d\lambda \qquad (3)$$

where $\hbar$ is the plank constant (6.623×10^{-34} J s^{-1}), c is the constant for the light speed (299,792,458 m s^{-1}), and N is Avogadro's number (6.022×10^{23}). $E_d(\lambda,z)$ was measured in µW m^{-2} nm^{-1}. The conversion from mol to µmol used a factor of 1×10^6.

The spectral coefficient for diffuse downwelling irradiation attenuation, $k_d(\lambda)$, at a geometric depth, defined as (Equation 4):

$$k_d(\lambda,z) = -\frac{1}{E_d(\lambda,z)}\frac{\partial E_d(\lambda,z)}{\partial z} \qquad (4)$$

was determined from in-water $E_d(z,\lambda)$ profiles following Mueller et al. (2003). The value for $k_d(\lambda)$ was computed as the local slope of $ln[E_d(z)]$ using a linear regression fit, and assuming a constant k_d within the interval $(z_m - \Delta z) \leq z \leq (z_m + \Delta z)$ where z_m is the center depth (Equation 5):

$$ln[E_d(\lambda,z)] = ln[E_d(\lambda,z_m)] - (z - z_m)k_d(\lambda,z_m) \qquad (5)$$

As proposed by Lee et al. (2005), $k_d(z)$ in the euphotic zone may be replaced by the integrated value of k_d from surface to a depth where E_d is reduced to approximately 1% or 10% of its surface value, i.e., k_d value in the layer between $E_d(0^-)$ and 1 or 10% of $E_d(0^-)$. Here, $k_d(E_d 10\%)$ was denominated as k_d because this layer contributes most to the water column photosynthesis and signals measured by remote sensors.

Nelson River and landfast ice introduce considerable quantities of minerogenic particles into Hudson Bay. To reduce the contribution to non-chlorophyllous particles that efficiently backscatter light, our analysis was restricted to the MIZ light environment. Water masses were classified using a cluster analysis applied to $k_d(\lambda)$, which is closely related to inherent optical properties (IOPs) and $[chla]$ (Solonenko and Mobley, 2015).

2.5. Phytoplankton photo-acclimation proxy

As mentioned in the Introduction, ocean optical properties can be used as proxies to assess phytoplankton photo-acclimation or size structure proxies (Huot et al., 2008; Devred et al., 2011; Brewin et al., 2012; Marañón, 2015; Fujiwara et al., 2018; Reynolds and Stramski, 2019). Here, we examined the potential of satellite-derived phytoplankton photo-acclimation proxies to better understand the state of the phytoplankton community characterizing the fall blooms. Our assessment is based on $[chla]$ and b_{bp}, which are important proxies for phytoplankton dynamics and pelagic ecosystems. While $[chla]$ is a direct proxy for phytoplankton, b_{bp} may be influenced by a wide range of non-chlorophyllous particles such as bacteria, micrograzers, heterotrophic nano-flagellates, ciliates, and viruses; organic particles of detrital origin such as fecal pellets and cell debris (non-living organic detritus derived from the

breakdown of micro-organisms); mineral particles of both biogenic (e.g., calcite liths and shells) and terrestrial origins (e.g., clays and sand); bubbles; and plastics (Vaillancourt et al., 2004; Bellacicco et al., 2019). Total b_{bp} therefore may be partitioned into two additive components:

$$b_{bp} = b_{bp}^{[chla]} + b_{bp}^k \qquad (6)$$

where $b_{bp}^{[chla]}$ is the backscattering component that co-varies with phytoplankton biomass and b_{bp}^k, the backscattering background that is due to non-algal particles (NAP) that do not co-vary with phytoplankton biomass.

To support our interpretations of b_{bp} as a phytoplankton proxy, we first needed to estimate b_{bp}^k. Behrenfeld et al. (2005) for example, estimated b_{bp}^k as the intercept of the least-squares regression analysis of the [chla] versus b_{bp} relationship. The backscattering background was considered as constant over the global ocean and fixed to a value of 0.00035 m⁻¹. More recently, however, Bellacicco et al. (2016) demonstrated that b_{bp}^k was not constant in either space or time scales in the Mediterranean Sea. Similar conclusions were drawn from an extensive analysis of global satellite ocean color data and in situ bio-ARGO data by Bellacicco et al. (2018; 2019), suggesting that b_{bp}^k variability must be considered in order to assess phytoplankton-related backscattering (or carbon content assuming a scaling factor, e.g., Behrenfeld et al., 2005). Therefore, we computed b_{bp}^k at 555 nm on a pixel-to-pixel basis using all daily satellite observations available for the 1998 to 2018 period for each month of open waters (May to October).

Values of b_{bp}^k were calculated as the background value of the relationship between b_{bp} and [chla] by fitting three methods: i) the linear model proposed by Behrenfeld et al. (2005); ii) the model presented by Bellacicco et al. (2019), which was first proposed by Brewin et al. (2012) to account non-linearity driven by phytoplankton size fractions; and iii) an exponential model that we propose with an offset to account for b_{bp}^k (Equation 7):

$$b_{bp}(555) = a \,[chla]^b + b_{bp}^k(555) \qquad (7)$$

where a and b are fitting parameters. The three fitting procedures were first tested on our in situ observations of b_{bp} and $[chla]_{HPLC}$ described above, as well as another data set from the Canadian Arctic (i.e., from Baffin Bay; results not shown).

Phytoplankton physiological adjustments to environmental conditions (e.g., light, nutrient status, taxonomy, stratification, and grazing) result in changes in the ratio of phytoplankton-carbon biomass (C_{phy}: in mg C m⁻³) to [chla] (Geider, 1987; Behrenfeld et al., 2005; Westberry et al., 2008; Sathyendranath et al., 2020). Therefore, assuming that phytoplankton dominates the covarying part of b_{bp}, as proposed by Behrenfeld et al. (2005), we estimated C_{phy} by multiplying $b_{bp}^{[chla]}$ by a fixed scaling factor (SF: 13,000 mg C m⁻²) (Equation 8):

$$C_{phy} = b_{bp}^{[chla]} \times SF = \left[b_{bp}(555) - b_{bp}^k(555) \right] \times SF \qquad (8)$$

3. Results
3.1. Monthly climatology of chlorophyll-a
Satellite ocean color monthly climatologies (1998–2018) of [chla] revealed the seasonal and spatial variability of phytoplankton in the HBS (**Figure 2**). In May, high [chla] (> 1 mg m⁻³) in open waters was a manifestation of ice-edge bloom. In June, concentrations remained high in most of the HBS also due to late ice-edge blooms, except in the central HB where oligotrophy was already established. The lowest [chla] were observed in August, except in coastal zones influenced by riverine inputs or where strong mixing processes (e.g., tidal mixing) operated year-long (i.e., in Hudson Strait). The trophic conditions revealed by satellite-derived [chla] are based on Barbedo et al. (2020) and Perrette et al. (2011) who defined the ice-edge bloom with [chla] greater than a threshold of 0.5 mg m⁻³ just after the ice retreat. The term oligotrophy is adopted for low [chla], as observed by Ferland et al. (2011) in summer in the HBS. Concentrations clearly began to increase again in September almost everywhere and continued to rise in October, including in the central HBS where oligotrophic conditions relaxed ([chla] increased from < 0.2 mg m⁻³ to > 0.5 mg m⁻³). We further examine in the next sections the physical processes potentially involved in explaining the late summer/fall increase in [chla] in the southern part of the oligotrophic area.

3.2. Atmospheric forcing, [chla], and b_{bp}: Seasonal and interannual variability
Figure 3 shows time-series of [chla], b_{bp}(555), wind speed, and heat flux between 2002 and 2009 in the south Hudson Bay (i.e., red box on **Figure 2** centered at location 84°W and 57°N). High [chla] during the spring-to-summer transition (June–July) was related to ice-edge blooms and, as a consequence, the stratification onset following the ice breakup. A reduction in [chla] was abrupt after the ice-edge bloom peak, following a decline in the ocean heating rate until south Hudson Bay reached a surface oligotrophic state (i.e., lowest [chla]). Chlorophyll-a concentration trends ($\partial \,[chla](\partial t)^{-1}$) indicated a systematic increase in [chla] between summer, with maximum oligotrophic state, and fall co-occurring with a seasonal process of atmospheric warming ocean decay (i.e., heat flux losing intensity). These trends were obtained by linear fit in the interval of confidence of 99% in 2003 (0.08 mg m⁻³ month⁻¹), 2005 (0.73 mg m⁻³ month⁻¹), 2006 (0.11 mg m⁻³ month⁻¹), 2007 (0.21 mg m⁻³ month⁻¹), 2008 (0.15 mg m⁻³ month⁻¹), and 2009 (0.25 mg m⁻³ month⁻¹). In 2002 and 2004, in contrast, [chla] time series remained flat at about 0.65 ± 0.26 and 0.48 ± 0.16 mg m⁻³, respectively. In addition to that, a sustained [chla] incremental increase during the summer-to-fall transition was observed in 2003, 2005 and 2007, just after the heat-flux inversion (positive to negative), i.e., when the ocean surface begin to cool (heat escaping the ocean).

The time evolution of b_{bp} was distinct from [chla], as b_{bp} presented a slight decrease during the spring-to-summer transition and remained relatively constant in summer. In fall, increases of b_{bp} had a small amplitude compared to [chla] (e.g., October 12 to 25, 2005 and 2007) or the b_{bp}
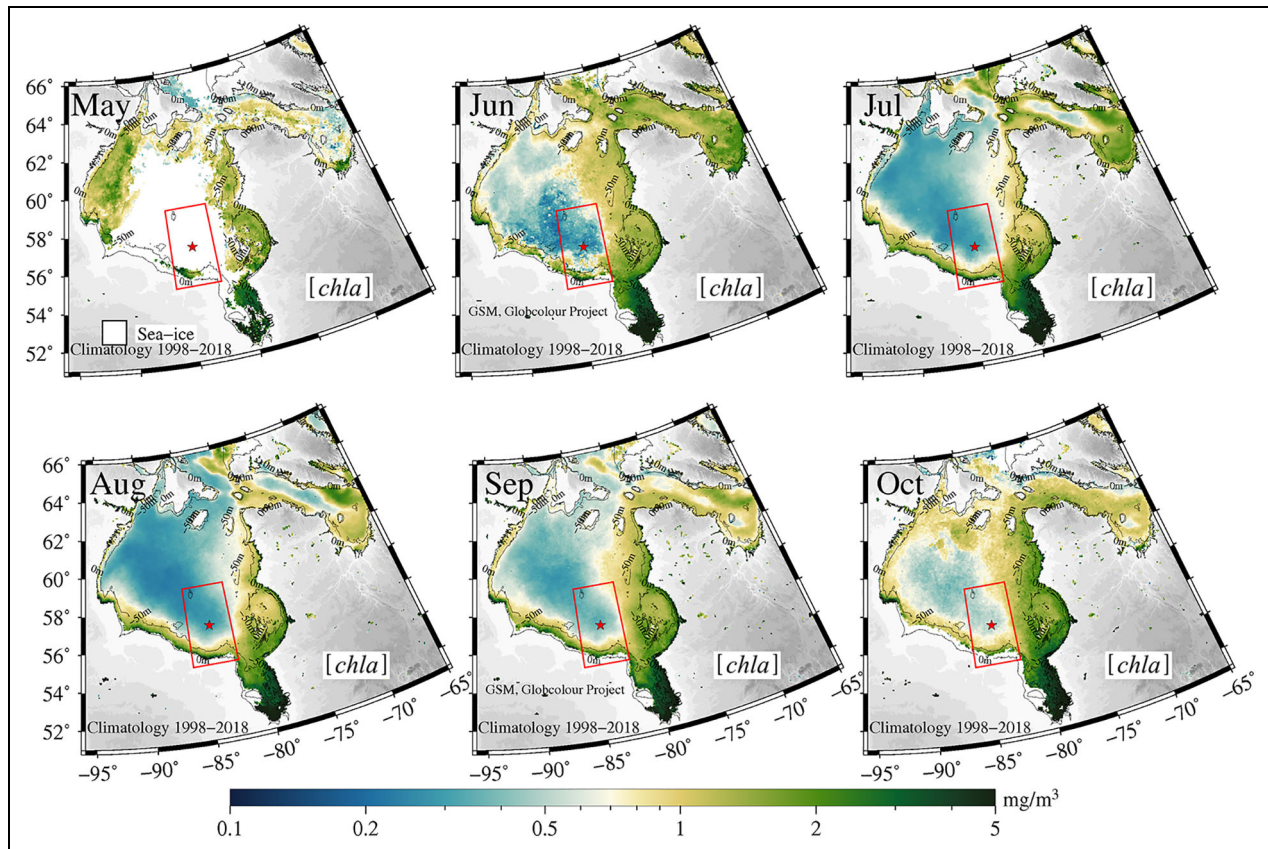
Figure 2. Climatology of chlorophyll-*a* concentration. Satellite ocean color monthly climatology (May, June, July, August, September, and October) of chlorophyll-*a* concentration ([*chla*]: color scale in mg m^{-3}) obtained between 1998 and 2018. The study area (red box) was centered on 84°W 57°N (red star) in South Hudson Bay where time series of [*chla*], wind speed, heat flux, and water column evolution were extracted in 2005.

time-series remained almost flat (e.g., 2002, 2003, 2006, 2008, and 2009).

Wind speed showed high variability, but its signature did not show a clear influence on [*chla*] (**Figure 3**). This mismatch between wind and [*chla*] were observed when wind components (zonal and meridional) were analyzed (Figure S2). The mismatch is particularly evident when high wind speed events (> 8 m s^{-1}) occurred and heat fluxes were positive. Such events were evident in late summer (August–September) and associated with a relatively low [*chla*] (e.g., 2002, 2003, 2004 and 2005) or followed by an ephemeral incremental increase in [*chla*]. Although strong wind events in summer, during positive heat flux, can result in an increase in [*chla*], as observed in 2003 (around August 13), they can also result in a decrease in [*chla*] (e.g., August 28 and September 27, 2003). For most years analyzed, peaks of wind speed during summer (between August 15 and September 15) were associated with [*chla*] lower than their respective phenological peaks. For example, when high wind speed (exceeding 6 m s^{-1}) was maintained between August 20 and September 12, 2007, [*chla*] remained low (< 0.8 mg m^{-3}) relative to the spring and fall blooms (2.0 mg m^{-3}).

In summary, wind speed versus [*chla*] links in late summer or fall were hard to detect because of the high wind-speed variability, i.e., ranging from 2 m s^{-1} to above 10 m s^{-1}

during a short time period, and because a large increment in [*chla*] often happened in the presence of moderate wind. However, strong wind events had more impact on [*chla*] when the ocean was cooling (e.g., 2005, 2007). Other factors such as heat fluxes and freshwater inputs have to be considered.

3.3. Correlation analysis: Chlorophyll versus atmospheric forcings

We extracted correlation coefficients between [*chla*] and wind speed (WS) or heat flux (HF) using a moving average filter with a time window ranging from 1 to 30 days applied to daily time series between 1998 and 2008. For each window range, WS and HF generated a pair of coefficients of correlation with [*chla*]. We segmented time series between pre-fall and fall seasons. The first day that the atmosphere-cooling ocean began (i.e., the day of heat-flux-inversion) defined the fall seasons. As a result, **Figure 4** shows a correlation analysis of [*chla*] with atmospheric forcing (WS and HF) on different time scales in southern Hudson Bay. In the spring-to-summer transition period, before the heat-flux inversion, wind speed and heat flux had a weak correlation outside the confidence interval of 95% (p < 0.05). After the heat-flux inversion, [*chla*] and wind speed reached a coefficient of correlation of 0.42 (p < 0.05), while [*chla*] and heat flux reached a high
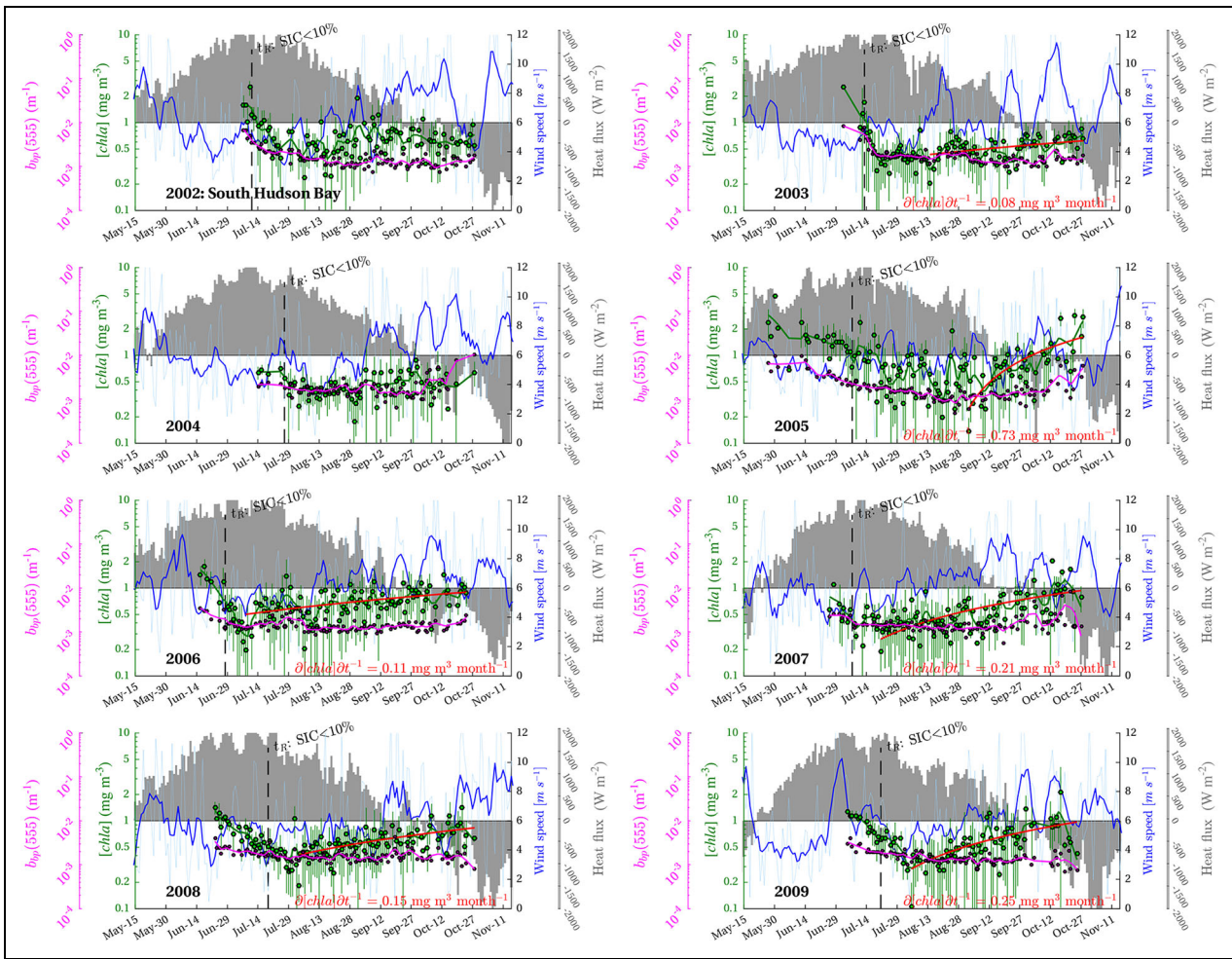
Figure 3. Phytoplankton dynamics and atmospheric forcing in South Hudson Bay. Time series of chlorophyll-*a* concentration ([*chla*], in mg m^{-3}, green circles; 7-day moving average, green line), backscattering coefficient at 555 nm (b_{bp}(555), in m^{-1}, magenta squares; 7-day moving average, magenta line) from the semi-analytical algorithm (GSM: Garver and Siegel, 1997; Maritorena et al., 2002) of the Globcolor project, wind speed (daily, in cyan line; 7-day moving average, blue line) from the Canadian Meteorological Centre's Global Deterministic Prediction System Re-Forecasts, and heat flux (gray bars) calculated by bulk formulas (Large and Yeager, 2004) using the NEMO Arctic and Northern Hemisphere Atlantic (ANHA4) with resolution of 0.25° between 2002 and 2009 in southern Hudson Bay (84°W and 57°N). The sea ice retreat day (t_R) was calculated using sea ice concentration (SIC) from the National Snow and Ice Data Center (NSIDC). Chlorophyll-*a* concentration trends (∂ [*chla*] $(\partial t)^{-1}$) in the 99% interval of confidence were plotted between maximum oligotrophic state in summer and fall (red line).

negative coefficient of correlation of -0.71 (p < 0.05) for the moving average filter of a 7-day window. The coefficient of correlation between [*chla*] and wind speed only had the confidence interval of 95% for a filter length of 7 days or longer, which indicated the low impact of high-frequency wind events on the phytoplankton dynamic.

3.4. Water column structure evolution
Figure 5A shows well-marked spring and fall blooms reaching 2 mg m^{-3} separated by an oligotrophic period of [*chla*] below 0.5 mg m^{-3} in 2005. The annual lowest sea surface salinity (< 29.5) and highest stratification ($N^2 \sim 1.5 \times 10^3$ s^{-1}) were reached on June 15 (**Figure 5B**), as a consequence of freshwater lenses produced by sea-ice melting and riverine input. After that date, there was a transition in the control of vertical stratification (i.e., β to α transition: Carmack and Wassmann, 2006; Carmack et al.,

2006) triggered on June 23, associated with the freshwater lens dissipation, mixed layer expansion, and pycnocline ventilation. The water column stratification, which was controlled mainly by the salinity gradient becomes controlled by the temperature gradient between July and August (**Figure 5C** and **D**). Pycnocline ventilation was fed continually with freshwater lens dissipation (**Figure 5B** and **C**). On August 10, the mixed layer depth (dashed line) definitively exceeded the first optical depth (z_{OC}, grey line), which was stably positioned around 10 m. The beginning of mixed layer expansion corresponded to the oligotrophic period of 2005 with lowest [*chla*] observed (< 0.2 mg m^{-3}). The [*chla*] decreased systematically following the ice-edge bloom dissipation from June 15 to August 18.

The phytoplankton fall bloom was observed as a systematic increase in [*chla*], coinciding with cooling throughout the water column and the heat-flux inversion observed on
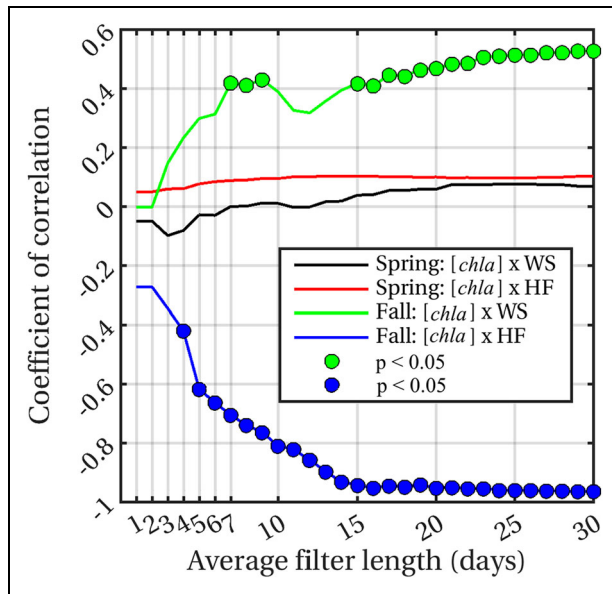
Figure 4. Response of phytoplankton biomass to atmospheric forcing on a range of time scales. Sensitivity analysis to assess the impact of heat flux and wind speed on chlorophyll-a concentration ([$chla$]) using an average filter length ranging in scale from 1 to 30 days in time series between 1998 and 2008 in southern Hudson Bay. The spring-to-summer transition was defined by the period before the heat flux inversion, and the summer-to-fall transition the period after heat-flux inversion, when atmospheric cooling of the ocean began. Coefficients of correlation of [$chla$] in relation to wind speed (WS) and heat flux (HF) with a confidence interval 95% are marked by solid green and blue circles, respectively.

September 11 (**Figure 5A**). The vertical gradients of temperature and salinity remained weak in the upper ocean layer (top 30 m) when an atmosphere-cooling ocean began. The heat-flux inversion also was coincident with the intercept between pycnocline and z_{eu} (**Figure 5A** and **B**). The abrupt increase in [$chla$] coincide with a decreasing trend in wind speed starting on October 5 (**Figure 5A**). Although [$chla$] observed during the fall blooms was similar to the spring-to-summer season in ice-edge booms, the dispersion of daily compared to 7-day averages revealed that the variability of [$chla$] in fall was clearly higher than in the ice-edge blooms (**Figure 5A**). Finally, an intensification of fall bloom was marked by another abrupt increase in [$chla$] (> 2 mg m^{-3}) after October 13 (**Figure 5A**), which was triggered by an intersection between the mixed layer and euphotic depth (**Figure 5B–D**), and ceased/collapsed by ocean freezing and sea-ice recovery.

3.5. Relationship between chlorophyll-a and particle backscattering coefficient
To gain further insights about the phytoplankton growing in the late summer and fall seasons, we first report the relationship between particle backscattering and chlorophyll-a measured in the field in summer. **Figure 6A** shows the relationship between in situ [$chla$]$_{HPLC}$ and $b_{bp}(555)$

obtained from field measurements in Hudson Bay in 2018. Stations were grouped in distinct light environments based on $k_d(\lambda)$ with high, moderate, and low light attenuation in marginal ice zones. Values for [$chla$]$_{HPLC}$ ranged from 0.1 to 15 mg m^{-3}, $b_{bp}(555)$ from 0.0004 to 0.02 m^{-1}, and $b_{bp}^*(555)$ from 0.0007 to 0.0506 m^2 (mg chla)$^{-1}$. These observations were used to test different fitting algorithms to estimate b_{bp}^k, before applying it to satellite ocean color data. As mentioned in Section 2.5, we compared the linear fit of Behrenfeld et al. (2005), the nonlinear least-squares algorithm of Bellacicco et al. (2019) and an exponential model (Equation 7). The later model performed better with r^2 of 0.760 ($rms.e = 0.001$, $n. = 37$), compared to r^2 of 0.707 and 0.30 for the Bellacicco et al. (2019) and Behrenfeld et al. (2005) models, respectively. The estimated b_{bp}^k using the exponential model yield values of 0.0023 m^{-1}, which is slightly higher than the value obtained using Bellacicco et al. (2019), and similar to the values obtained with the linear fit. Similar results and conclusions were obtained in Baffin Bay (results not shown).

The carbon-to-chlorophyll ratio estimated after the application of Equations 8 and 7, C_{phy}:[$chla$]$_{HPLC}$, yielded a mean value of 17.31 and maximum value of 120. **Figure 6B** shows chlorophyll-specific backscattering at 555 nm ($b_{bp}^*(555)$ in m^2 (mg chla)$^{-1}$) as a function of [$chla$]$_{HPLC}$ in distinct light levels (colored symbols). As reported for high latitudes (Reynolds et al., 2001; Stramska et al., 2003; Wang et al., 2005; Zhuang et al., 2020), we observed an inverse relationship between $b_{bp}^*(555)$ and [$chla$]$_{HPLC}$.

3.6. Satellite-derived phytoplankton photoacclimation proxy
Besides [$chla$] (**Figure 2**), ocean color satellite monthly climatologies revealed the seasonal and spatial variability of particle backscattering in the HBS, which is assumed to respond both phytoplankton and non-algal particle concentrations. The monthly climatology of $b_{bp}(555)$ (**Figure 7**) shows the highest values (> 0.002 m^{-1}) near the coast, simultaneously with the seasonal peak of river runoff and ice melting between May and June. The b_{bp} was maximum in May (mean ± standard deviation: 0.0025 ± 0.0005 m^{-1}, n = 12312) and June (0.0022 ± 0.0006 m^{-1}, n = 60957), decreased in July (0.0019 ± 0.0006 m^{-1}, n = 69238), and remained constant in August (0.0016 ± 0.0005, n = 70813), September (0.0016 ± 0.0005 m^{-1}, n = 70841) and October (0.0016 ± 0.0005 m^{-1}, n = 62450).

Similar to Bellacicco et al. (2020), $b_{bp}^k(555)$ was estimated by applying Equation 7 to all satellite daily observations available for a given month between 1998 and 2018, and for a given 4.5-km resolution pixel. The spatially resolved $b_{bp}^k(555)$ monthly maps are shown in **Figure 8** and statistics for the whole HB in boxplot in Figure S9. The seasonal minimum coincided with fall blooms in September (0.0004 ± 0.0004 m^{-1}, n = 70839) and October (0.0002 ± 0.0003 m^{-1}, n = 62442), and ice-edge blooms in May (0.0004 ± 0.0005 m^{-1}, n = 12304). Seasonal low contribution of NAP to total backscattering (b_{bp}^k:b_{bp}) also occurred in May (14.6%) and October (13.8%). The $b_{bp}^k(555)$ reached the seasonal peak after the
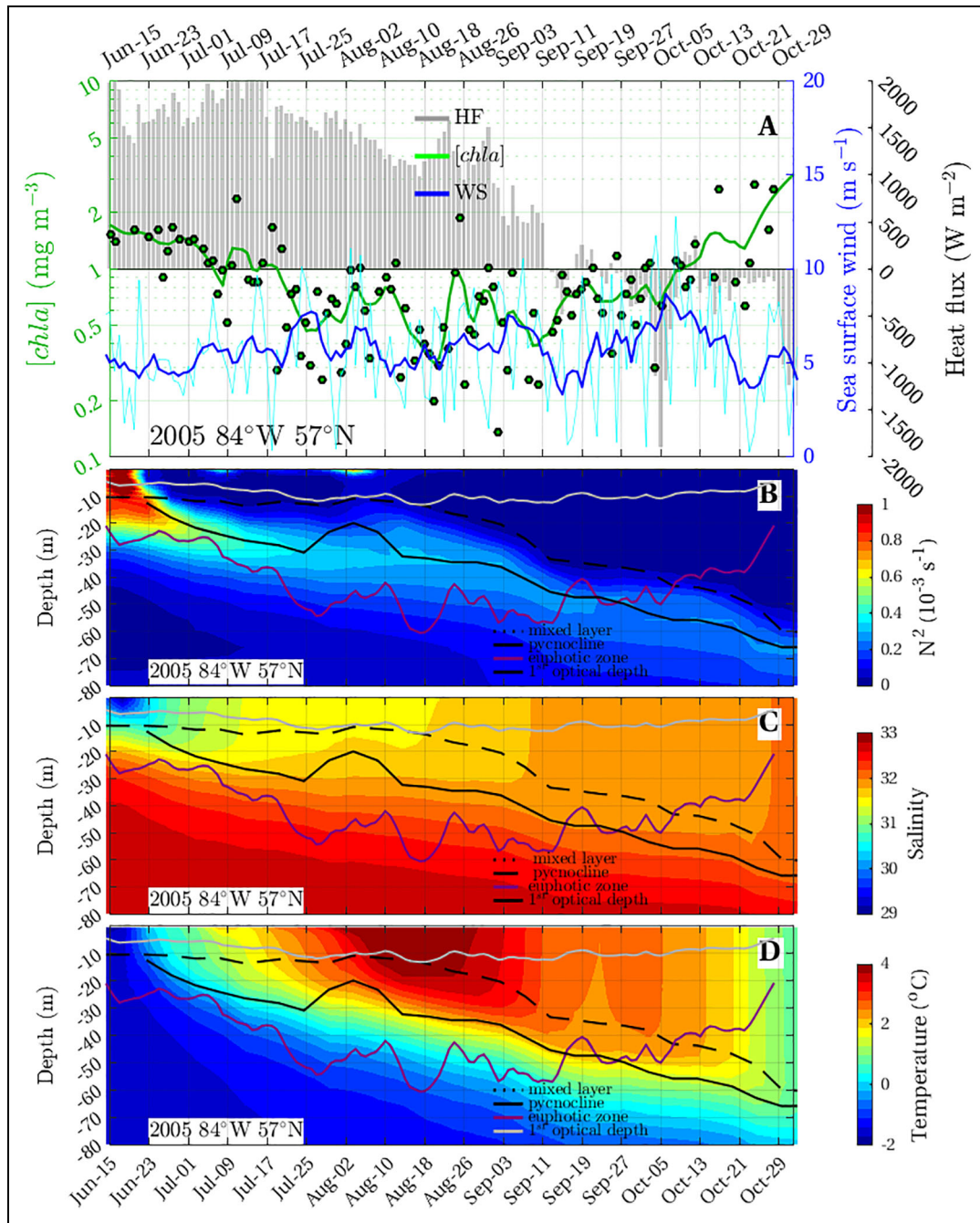
Figure 5. Synergy of sea-ice model, wind speed reanalysis, and ocean color satellites in South Hudson Bay, 2005. Influence of atmospheric forcing and water column structure on phytoplankton phenology in southern Hudson Bay at 84°W and 57°N in 2005: (A) time series of [chla] from Globcolor Project (GSM: Garver and Siegel, 1997; Maritorena et al., 2002) in log scale (daily, green squares; 7-day moving average, green line), heat flux (HF, grey bars) and wind speed (daily, cyan line; 7-day moving average, blue line). Profiles in color scale of (B) Brunt-Vaissala frequency (N^2), (C) salinity, and (D) temperature. The important layers for phytoplankton dynamics are marked on vertical profiles: satellite-derived first optical depth (z_{OC}, white line) and euphotic zone depth (z_{eu}, purple line); mixed layer depth (MLD: black traced line); and pycnocline (N^2_{max}, black line).

ice-edge bloom season in July (0.0006 ± 0.0007 m^{-1}, n = 69238), simultaneous with its peak of NAP contribution to total backscattering (b^k_{bp}:b_{bp} of approximately 36.2%).

Monthly phytoplankton carbon, C_{phy}, was estimated by subtracting b^k_{bp} (**Figure 8**) from b_{bp} (**Figure 7**) and multiplying by a scaling factor of 13,000 mg C m^{-2} (Equation 8)

(Behrenfeld et al., 2005; Bellacicco et al., 2020). The seasonal patterns in C_{phy} (**Figure 9**) slightly differ from [chla] (**Figure 2**) and b_{bp} (**Figure 7**). In general, C_{phy} was higher than 27.9 mg C m^{-3} in May and 21.1 mg C m^{-3} in June during the ice-edge bloom, then decreased to reach a minimum in August (< 12.4 mg C m^{-3}). During the summer months, C_{phy} remained high in the southern HBS and in
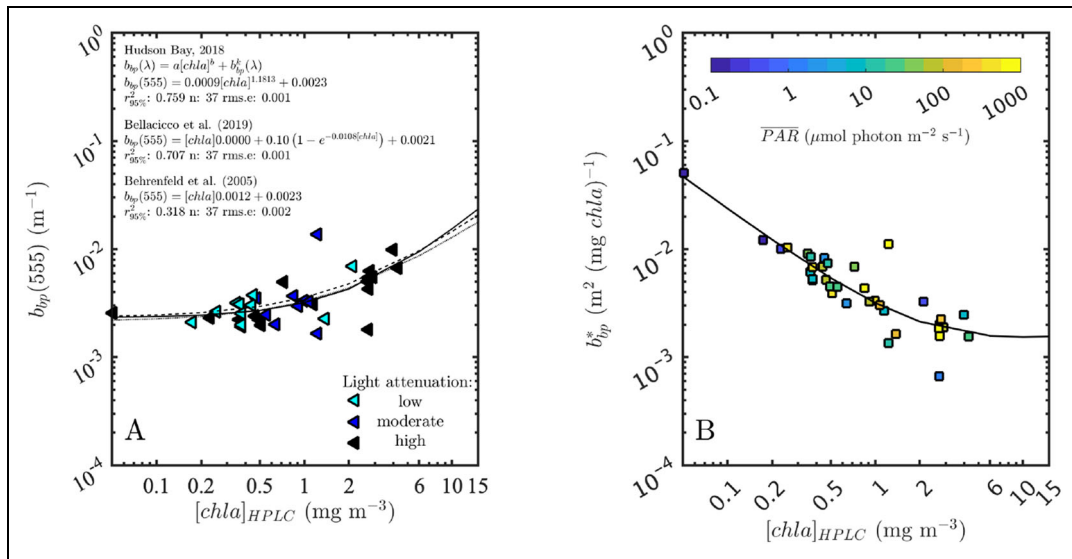
Figure 6. Chlorophyll-*a* concentration, light backscattering coefficient and photosynthetic active radiation interplay in the Eastern Canadian Arctic. Scatter plots of in situ coincident chlorophyll-*a* concentration ($[chla]_{HPLC}$, in mg m^{-3}) measured using high-performance liquid chromatography (HPLC) and particulate backscattering coefficients ($b_{bp}(555)$, in m^{-1}) by ECO BB9 in Hudson Bay in 2018 (A). Distinct light environments in the marginal ice zone (MIZ) were grouped based on light attenuation, $k_d(\lambda)$ (high, cyan triangles; moderate, blue triangles; low, black triangles). The b_{bp}-chla relationships were fitted using models proposed by Behrenfeld et al. (2005; dotted line), Bellacicco et al. (2019; dashed line), and an exponential equation with offset (this study; black line) to account the non-algal background backscattering (b_{bp}^k). (B) chlorophyll-specific backscattering ($b_{bp}^*(555)$, in m^2 (mg chla)$^{-1}$) as a function of $[chla]_{HPLC}$, and daily average photosynthetic active radiation ($\overline{PAR}$, in color scale) in Hudson Bay (squares).
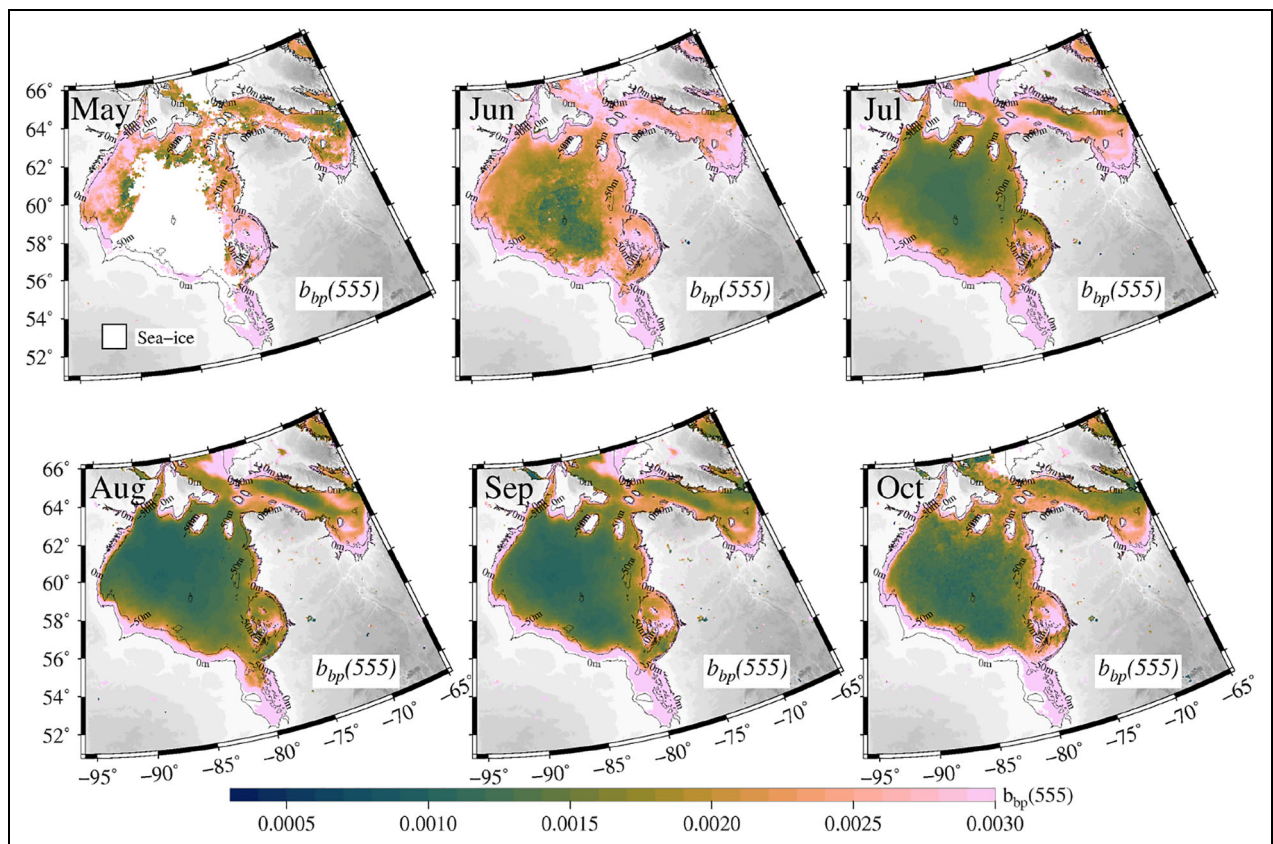
Figure 7. Climatology of total backscattering coefficients. Satellite ocean color monthly climatology (May, June, July, August, September, and October) of the total particle backscattering coefficient at 555 nm, $b_{bp}(555)$, obtained between 1998 and 2018.
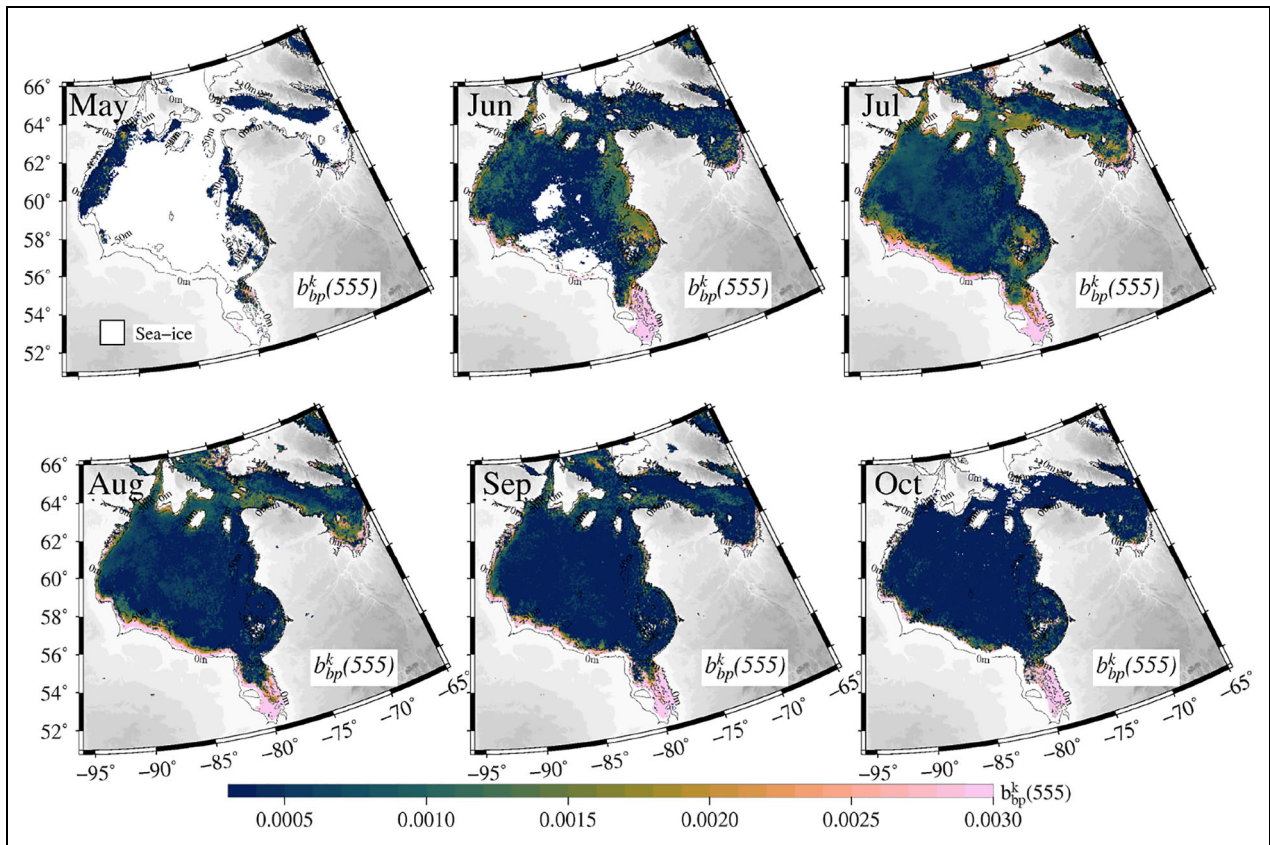
Figure 8. Climatology of non-algal backscattering coefficients. Satellite ocean color monthly climatology (May, June, July, August, September, and October) of the non-algal particle backscattering coefficient at 555 nm ($b_{bp}^k(555)$, in m^{-1}) obtained between 1998 and 2018, estimated from the relationship between satellite-derived $b_{bp}(555)$ and [$chla$].

coastal waters of Hudson Strait. An overall increase in C_{phy} was observed in September (15.7 $\pm$ 5.9 mg C m^{-3}, n = 70841, and during fall blooms in October (18.3 $\pm$ 5.9 mg C m^{-3}, n = 62450; Figure S9).

The seasonal variability of [$chla$] and C_{phy} resulted in considerable seasonal variability in the C_{phy}:[$chla$] ratio (**Figure 10**). Here, we present the seasonal evolution of this parameter, which is known to reflect phytoplankton photoacclimation, nutrient availability, and temperature (Geider, 1987; Geider et al., 1997; Sathyendranath et al., 2009; Jakobsen and Markager, 2016). In May, the phytoplankton found in the marginal ice zone presented high concentration of carbon (C_{phy}: 27.2 $\pm$ 7.9 mg C m^{-3}, n = 12312) and chlorophyll-a ([$chla$]: 1.13 $\pm$ 0.44 mg m^{-3}, n = 12312). The [$chla$] higher than 2 mg m^{-3} dominated the open water regions near the coasts, with maximum C_{phy} (> 20 mg C m^{-3}) observed in polynyas, i.e., in the Northwest Hudson Bay and south of Belcher Islands. C_{phy}:[$chla$] ratios were particularly low along the ice edge in the northwest polynya. C_{phy}:[$chla$] increased systematically offshore from May to June. High C_{phy}:[$chla$] (> 40) coincided with maximum annual solar flux (summer solstice), and remained high in oligotrophic regions in the central HBS until August. Relatively low C_{phy}:[$chla$] values were found in eastern HB and in coastal waters of the Hudson Strait where high [$chla$] was also evident (**Figure 2**). From August to October, C_{phy}:[$chla$] tended to decrease

everywhere in the HBS, except in some coastal zones (e.g., Ungava Bay). The seasonal minimum was reached in October (22.0 $\pm$ 7.2, n = 62450) with values lower than those observed during the spring bloom in May (26.5 $\pm$ 9.7, n = 12312). At this time of the year, the phytoplankton contribution to backscattering (b_{phy}:b_{bp}) was largest (approximately 86%).

4. Discussion
4.1. Phytoplankton fall bloom onset
How is the phytoplankton fall bloom triggered and maintained in Hudson Bay? The synergy of the ocean color satellite data, sea-ice dynamic model output, climatic reanalysis, and in situ bio-optic profiles underscores the influence of atmospheric forcing and water-column evolution on phytoplankton dynamics.

4.1.1. Role of freshwater
As observed in **Figure 5**, analogous to other years presented in Figures S3–S8, the seasonal evolution of the water-column structure follows these stages: 1) freshwater lens dissipation during summer; 2) vertical displacement between mixed layer and pycnocline; 3) mixed layer expansion and pycnocline ventilation; 4) a transition between a β (haline) to α (thermal) stratification; and 5) euphotic depth reaching the pycnocline and, subsequently, the depth of the mixed layer.
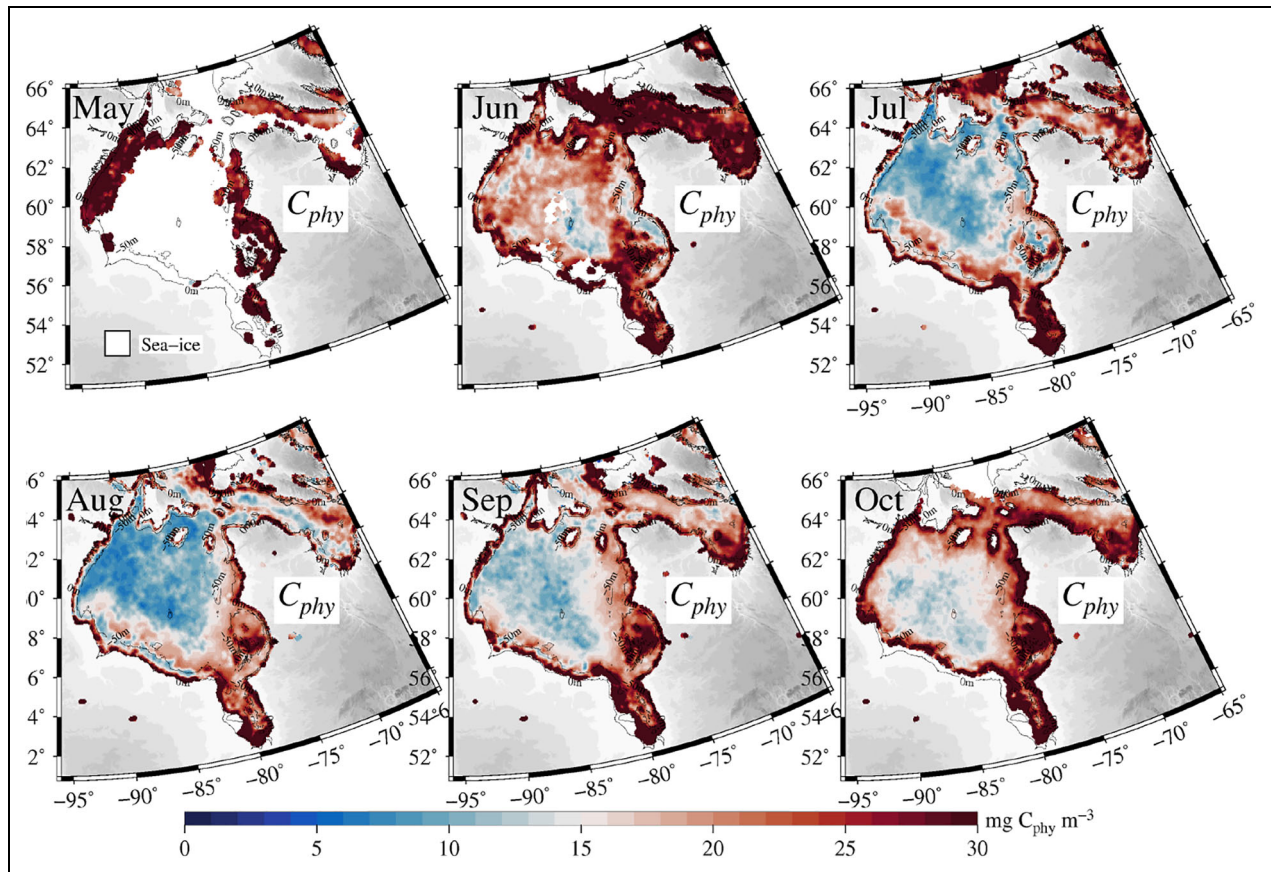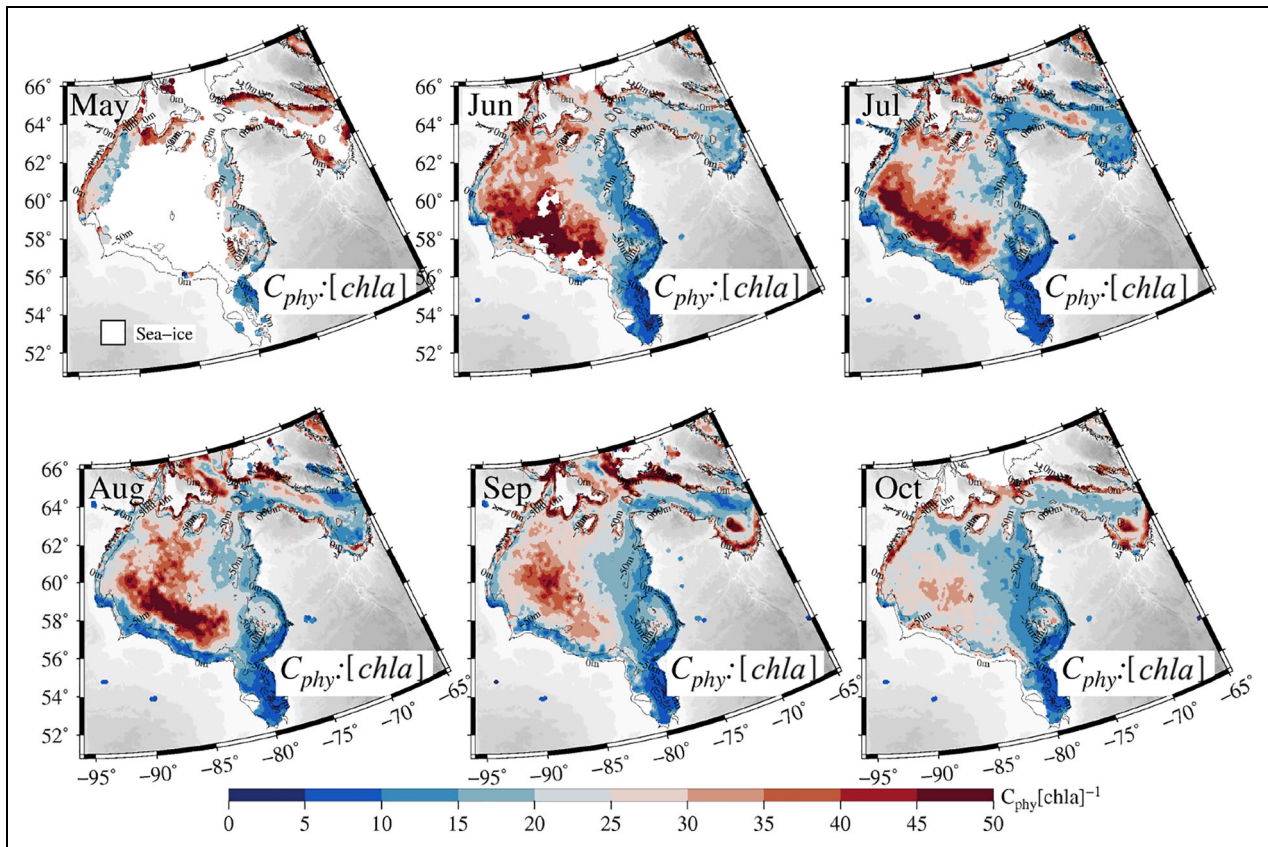
Figure 9. Climatology of phytoplankton carbon. Satellite ocean color monthly climatology (May, June, July, August, September, and October) of the total phytoplankton carbon (C_{phy}: in mg C m^{-3}) obtained between 1998 and 2018 in Hudson Bay.

Climatic maps of [$chla$], C_{phy}, and C_{phy}:[$chla$] (**Figures 2, 9** and **10**), revealed that the ice-edge blooms in the spring-to-summer transitions and the rise in phytoplankton in the summer-to-fall transitions were productive features interrupted by a relatively severe oligotrophy. This oligotrophic period was defined by a high seasonal C_{phy}:[$chla$] ratio in regions of [$chla$] below 0.5 mg m^{-3}, which occupied more than 50% of the bay. Ice-edge and fall blooms are very distinct from each other in terms of water column structure, stratification, and heat flux. In spring, the freshwater lens produced the highest annual stratification near the sea surface, while mixed layer expansion and pycnocline ventilation affected the whole euphotic layer in fall.

As presented in **Figure 5**, the annual maximum of stratification coincided with the seasonal peak of riverine input and ice melting in June and July (Prinsenberg, 1984). According to Déry et al. (2005), riverine inflow can exceed 4 km^3 day^{-1} in midsummer. In the upper layer, freshwater lenses (salinity < 30) produced strong stratification, which held both the mixed layer and pycnocline close to the surface layer (approximately 10 m; Stewart and Lockhart, 2005; Granskog et al., 2011). After the seasonal peaks of ice-melting and continental drainage (Prinsenberg, 1984; Déry et al., 2005), the dissipation of freshwater lenses triggered a continuous process of pycnocline ventilation and mixed-layer

expansion until sea surface freezing at the end of autumn (**Figure 5**). Meanwhile, after the peak of heat flux (atmospheric warming ocean) and sea-ice retreat, the vertical stratification, previously controlled by salinity gradients, was then switched by temperature gradient, i.e., it switched from β to α stratification (Carmack and Wassmann, 2006; Carmack et al., 2006). As discussed by Carmack and Wassmann (2006) and Carmack et al. (2006), phytoplankton production and vertical distribution of chlorophyll in thermal-stratified (α stratification) polar seas is more sensitive to mixing and convection than salinity-stratified (β stratification) shelves dominated by freshwater.

The pre-fall-bloom stage occurred when the euphotic zone became shallower until it found the maximum stratification layer, which was getting deeper response to pycnocline ventilation, and when [$chla$] had risen from 0.4 to 0.9 mg m^{-3} between September 11 and 19, 2005, the beginning of the heat-flux inversion period. Then, a massive increase in [$chla$] was triggered when mixed layer expansion reached z_{eu}. When this stage was reached, the euphotic layer and whole phytoplankton productivity layer became confined to the mixed layer, characterized by weak stratification and homogeneous profiles of salinity and temperature. Similar to observations reported by Fujiwara et al. (2018) in the Chukchi shelf, wind-driven and convective turbulence intensified the erosion of water

Figure 10. Climatology of ratio of phytoplankton carbon to chlorophyll. Satellite ocean color monthly climatology (May, June, July, August, September, and October) of the ratio of phytoplankton carbon to chlorophyll-a concentration (C_{phy}:[$chla$]) obtained between 1998 and 2018. C_{phy} was computed using the backscattering coefficient of non-algal particles at 555 nm, $b_{bp}^{\kappa}(555)$, spatially resolved at pixel scale. The values of $b_{bp}^{\kappa}(555)$ were estimated by the Bellacicco et al. (2019) method using satellite-derived $b_{bb}(555)$ and [$chla$] calculated from the semi-analytical algorithm (GSM: Garver and Siegel, 1997; Maritorena et al., 2002) of the Globcolor Project merged daily 4-km products.

column structure in south Hudson Bay. Subsequently, the fall bloom development, defined by a significant increase in [*chla*], followed homogenization of the whole productive layer (**Figures 5** and S3–S8).

In south Hudson Bay, NEMO modeling revealed high interannual variability of freshwater input, with years when surface salinity was low (2006, 2007, and 2008; Figures S6–S8) and years when it was high (2002 and 2004; Figures S3 and S5). As a result, the response of phytoplankton to atmospheric forcing will depend on freshwater inputs, which vary from year to year. Riverine input can increase the stocks of nutrients and remineralization in the whole bay. However, freshwater counteracts brine rejection blocking the upward flux of nutrients from the deep nutrient pool in winter (Eastwood et al., 2020). Phytoplankton can rapidly assimilate nutrients from rivers, which confines high production only to coastal areas and river plumes in summer (Kuzyk et al., 2010; Jacquemot et al., 2021). Indeed, the interannual variability of complex interplays of nutrient inventories, an atmospheric-heating ocean, and wind-driven turbulence throughout summer are pre-conditions for the phytoplankton dynamics in the fall season. For example, years of predominantly low upper-layer stratification (e.g., 2006) can allow nutrient replenishment in the euphotic

layer, sustaining an increase of chlorophyll throughout the summer but weakening an eventual fall bloom triggered by convection due to prior depletion of the subsurface nutrient pool. On the other hand, strong stratification counteracts vertical transport of nutrients from below the euphotic zone and reinforces oligotrophy. The SCM responds directly to water column structure in Hudson Bay as discussed by Sibert et al. (2010; 2011), Ferland et al. (2011), Estrada et al. (2012), and Lapoussiere et al. (2013). In summer, water column structure can restrict phytoplankton production in the sub-surface chlorophyll-*a* maximum causing a nutricline deepening at levels below the range of convection-driven turbulence, which will dampen the fall bloom process (e.g., 2002 and 2004).

4.1.2. Role of winds and heat fluxes

Turbulent mixing is a key to understanding the bloom onset. As reported by Falkowski and Oliver (2007), the climate-driven processes that influence turbulent mixing in the ocean seem to have strongly influenced the diversity and relative abundance of the major eukaryotic phytoplankton taxa in the geological (Phanaerozoic Eon) and contemporary ocean (Anthropocene). Sources of turbulence in the upper layer occur over a wide range of spatial and temporal scales, and result in non-homogeneous

vertical distribution of turbulence in the mixed layer. As detailed by Franks (2015), turbulence in the ocean is a result of energy dissipation through the following processes: wind, waves, Langmuir circulation, and convectively driven turbulence. Both wind-driven and convection-driven (heat-fluxes) processes were examined for fall bloom onset in HB (**Figures 4** and S2). The convection impacts uniformly and strongly the mixed layer defining the seasonal pycnocline. Otherwise, wind-driven turbulence is likely dominant in the upper layer, decays with depth, and dissipates in a short time scale (hours or less). Wind-driven turbulence can impact negatively phytoplankton production in the upper layer, especially in the first optical depth, (Behrenfeld, 2010; Taylor and Ferrari, 2011; Fischer et al., 2014; Franks, 2015). In polar seas, an increase in annual phytoplankton production is assumed, in part, to be caused by storm events that drive turbulence in the upper ocean layer (Ardyna et al., 2013; Fujiwara et al., 2018). However, a direct link between storms and fall blooms is not a general consensus, as pointed by Sigler et al. (2014). In Hudson Bay, sea-surface wind events only have a direct impact on [chla] after heat-flux inversion, i.e., when the atmosphere began to cool the upper-ocean layer (**Figure 3**). However, the increase in [chla] after the HF inversion is not systematic and probably depends on the nature of the stratification (α versus β stratification), i.e., the presence of freshwater in the upper ocean.

As discussed by Kim et al. (2007) for the Japan/East Sea and by Olita et al. (2014) in the Mediterranean Sea, the phytoplankton response takes some time to assimilate a new supply of nutrients introduced into the upper ocean layer. However, lagged correlations between wind speed and [chla] were not statistically significant in this study. Otherwise, convection-driven turbulence has a homogeneous effect on the whole mixed layer that determines its seasonal depth. As reported by Ferland et al. (2011) in summer (August and September), the depths of the nutricline and sub-surface chlorophyll-a maximum are very close to the euphotic zone depth in Hudson Bay. Therefore, convection-driven turbulence results in the mixed layer expansion and pycnocline ventilation, potentially releasing nutrients and phytoplankton communities from the SCM into the upper euphotic layer. The freshwater input and sea-ice melting impact the resilience of the water column structure against wind-driven turbulence because freshwater shields the upper-layer structure, and the absence of convection dampens the bloom development, as observed in situ during the summer-to-autumn transition on the northern Chukchi Sea (Nishino et al., 2015). Although nutrient resupply by Ekman pumping is an important factor in increasing phytoplankton production, excessive turbulence and mixing can have a negative effect. As demonstrated by Franks (2015), wind-driven turbulence strongly affects the upper layer but loses efficiency with depth. In addition, the restructuring of stratification in response to the wind-driven turbulence is a much faster process than the restructuring in response to convection (Franks, 2015).

The negligible impact on [chla] in response to persistent strong winds and high frequency wind events

(**Figure 3**), coastal upwelling (Enriquez and Friehe, 1995) forced by winds parallel to coastal line orientation (Figure S2) and in the ice-edge (Dumont et al., 2010), or in the absence of convection prior to heat flux inversion (**Figure 4**), supports the idea that fall blooms are triggered when convective-driven turbulence begins to erode stratification. Specifically, wind-driven mixing alone can be more effective in limiting phytoplankton production in the first optical depth than in promoting it by nutrient transport via Ekman pumping. As presented in the section on the ice-ocean model and heat-flux calculations (Methods), the wind has a direct effect on heat flux. Although wind speed is key to understanding how atmospheric forcing impacts phytoplankton dynamics, our results highlight the importance of atmospheric cooling of the surface ocean on stratification. We found that the water column stratification resisted wind-driven turbulence events until the atmosphere effectively began to cool the ocean, producing a systematic increase in [chla].

4.2. Phytoplankton photoacclimation

As mentioned in Methods, phytoplankton physiological adjustments to environmental conditions result in changes in the ratio of phytoplankton-carbon biomass to [chla]. We estimated C_{phy} from satellite-derived particle backscattering after considering the non-algal backscattering background. We first discuss this backscattering background, followed by the use of C_{phy}:[chla] as a proxy to investigate the seasonal evolution of phytoplankton photoacclimation, and how this ratio informs the productivity of fall blooms.

4.2.1. Contribution of non-algal particles to total backscattering

All matter in the ocean scatters light, whether water molecules, sea-salt ions, or particles (Zhang et al., 2020). Natural aquatic assemblages have a variable pool of particle size, shape, and composition (organic/inorganic), which limits our ability to correctly interpret ocean color satellite observation of b_{bp} in terms of phytoplankton photophysiological aspects (Organelli et al., 2018; Koestner et al., 2020). Uncertainties on the use of b_{bp} to infer phytoplankton community composition derive from the intricate effect of non-algal particles composed of heterotrophic organisms, organic detritus (e.g., fecal pellets, and cell debris), and inorganic sediments (e.g., clays, sand, calcite, and liths). For example, inorganic particles generally dominated the backscatter of assemblages because of the high refractive index of minerogenic particles, compared with organic-dominated assemblages (Effler et al., 2013; Reynolds et al., 2016; Koestner et al., 2020). Optically complex waters exhibit diverse particle types where phytoplankton and NAP represent varying proportions of the suspended particle pool, subject to potentially large and independent variations (Reynolds and Stramski, 2019). In order to gain more insights about phytoplankton-related backscattering, we assessed from satellite ocean color data the NAP contribution on a pixel basis using an approach similar to that proposed by Bellacicco et al. (2018; 2020). The satellite-derived b_{bp}^k is

the contribution of NAP to b_{bp} that does not covary with [*chla*]. Based on field observations, b_{bp}^k was calculated using an exponential equation with offset (**Figure 6**), which performed better than the non-linear model proposed by Bellacicco et al. (2019) or the linear model of Behrenfeld et al. (2005). More importantly, we showed that b_{bp}^k varies in space and time (**Figures 8**, S9, and S10) with the highest values obtained after the ice-edge bloom (in June or July, excluding the nearshore coastal waters) reaching a contribution to b_{bp} of about 35%. This result may reflect the production of non-algal particles such as micrograzers, bacteria, viruses, cell debris and fecal pellets during post-bloom conditions. This contribution of NAP, however, is relatively low compared to the global ocean, but similar to that reported in the productive waters of the North Atlantic (Bellacicco et al., 2018). At the ice edge in May, for example, we observed low b_{bp}^k:b_{bp} (Figure S9) and high [*chla*], which could have involved two processes: i) fast-sinking aggregates of ice algae and sympagic communities that quickly remove NAP from the pelagic to the benthic realm (Lannuzel et al., 2020; Trudnowska et al., 2021); and ii) early ice retreat that results in a faint manifestation of under-ice and ice-edge blooms (Barbedo et al., 2020).

4.2.2. Satellite-derived C_{phy}:[*chla*] proxy

Provided that a satellite climatology successfully described the seasonality of b_{bp}^k and b_{bp} in HBS, C_{phy}:[*chla*] appeared as a robust proxy to investigate the seasonal evolution of phytoplankton community size structure and photophysiology in the summer-to-fall transition. However, we recognized that the conversion of b_{bp} to phytoplankton carbon may be controversial, as isolating the backscattering signal from phytoplankton cells alone (or phytoplankton carbon from POC) from bulk measurements in the natural environment is not possible (Sathyendranath et al., 2009). Therefore, C_{phy} includes the contribution of all particles that co-varied with [*chla*]. Absolute values of C_{phy}:[*chla*] reported here (**Figure 10**) in spring and fall seasons, or in coastal waters, are in the lower range compared to the literature in the open ocean (Sathyendranath et al., 2009; Bellacicco et al., 2016), but similar to the range reported for coastal waters of the North Baltic Sea (same latitude as the HB; ratios of 10–60; Jakobsen and Markager, 2016). A phytoplankton population composed of smaller cells backscatters more light than one composed of larger cells, for an equal amount of chlorophyll present (Vaillancourt et al., 2004; Reynolds et al., 2016; Koestner et al., 2020). Low values of C_{phy}:[*chla*] probably indicate the presence of larger cells with low backscattering efficiency and high chlorophyll-*a* content that are typically found in low light environments and/or nutrient-replenished (mesotrophic or eutrophic) environments (Devred et al., 2006; Barbieux et al., 2018).

4.2.3. C_{phy}:[*chla*] seasonal variability

As shown in **Figure 10**, the highest seasonal values of C_{phy}:[*chla*] were associated with oligotrophy in the summer. Therefore, satellite ocean color observations highlighted the photo-acclimation strategy of phytoplankton

communities to deal with the high summer irradiance and nutrient depletion in the upper layer of the HBS. Satellite observations and vertical profiles acquired in the spring-to-summer transition help to improve our understanding about phytoplankton dynamics. In situ empirical relationships between $b_{bp}(555)$, [*chla*], and PAR in distinct light-attenuation environments of the MIZ revealed that phytoplankton communities in the upper layer at high PAR levels had a relatively low intracellular pigment content and small size structure and, consequently, high $b_{bp}^*(555)$ and C_{phy}:[*chla*] (**Figure 6**). As reported by Westberry et al. (2008), for example, upper layer phytoplankton communities generally have low pigment content and small size structure cells to better deal with relatively high PAR, poor nutrient supply, and high wind-driven turbulence. On the other hand, the phytoplankton community around the SCM is photo-acclimatized to a balance between low PAR, relative high nutrients, high stratification and low turbulence, which results in relatively large cells and high intracellular chlorophyll-*a* content, i.e., relatively low $b_{bp}^*(555)$ and C_{phy}:[*chla*] (Brewin et al., 2012; Barbieux et al., 2018).

During the fall season, a decrease of C_{phy}:[*chla*] and negligible stratification in the productive layer may indicate an advection/seeding of SCM communities to the first optical depth. Otherwise, climatology-depicted photoacclimation as a seasonal process was synchronized with solar elevation and nutrients in Hudson Bay. For example, low C_{phy}:[*chla*] in an ice-edge bloom is likely due to high nutrient availability in a shallow mixed layer under the maximum seasonal light incoming in May and June. In summer, high C_{phy}:[*chla*] indicated the presence of small phytoplankton cells with relatively low intracellular chlorophyll pigments in oligotrophic domains under high PAR (**Figures 2** and **9**). Although very distinct water column structures are involved in ice-edge and fall blooms, in general similar and relatively low C_{phy}:[*chla*] characterized spring and fall, intercalated with a smooth transition through maximum C_{phy}:[*chla*] in domains of severe oligotrophy during summer. Phytoplankton photoacclimation, size structure, and community were similar in ice-edge and fall blooms, (**Figures 2**, **9**, and **10**). In addition, a seasonal increment of C_{phy} together with [*chla*] (**Figures 2** and **9**) and a decrease of b_{bp}^k (**Figures 8**) and its relative contribution to b_{bp} (Figures S10 and S9) support the hypothesis of a productive fall bloom.

5. Conclusions

The present study achieved a synergy between hydrodynamic modeling, climate reanalysis, ocean-color imagery, and in situ observations to better understand fundamental aspects of phytoplankton dynamics, with special attention dedicated to the fall bloom phenomenon. Atmospheric cooling of the ocean and wind-driven turbulence can facilitate the transport of nutrients by mixed-layer expansion and pycnocline ventilation after the heat-flux inversion, when the atmospheric cooling of the ocean began. However, the interplay of phytoplankton and atmospheric forcing is not straightforward in a region where both haline and thermal processes affect water-column stratification.

Satellite-based optical proxies revealed that phytoplankton communities with a low carbon-to-chlorophyll ratio observed at the surface in the fall may be advected from the subsurface chlorophyll-*a* maximum to the depth visible by spaceborne sensors. However, the significant increase in phytoplankton-related carbon concentration (while non-algal backscattering remained constant) indicated that these fall blooms are potentially productive. To quantify the relative importance of fall blooms in Arctic and sub-Arctic seas, the carbon-to-chlorophyll ratio can improve the parameterization of phytoplankton primary production from satellite or coupled biogeochemical models (International Ocean Colour Coordinating Group, 2015; Sathyendranath et al., 2020).

The persistence of fall blooms can enhance the carbon pump and mitigate Arctic warming by removing greenhouse gases (carbon dioxide). However, the biogeochemical capability of the Arctic and sub-Arctic seas to assimilate both a high content of organic matter discharged by rivers and that produced in situ by phytoplankton blooms in a rapidly changing Arctic scenario remains an open topic.

Data accessibility statement
The day of in situ backscattering coefficient and chlorophyll-*a* concentration in this research are made available through the BaySys data repository DOI: https://dev.unimanitoba.links.com.au/data/project/baysys.

Supplemental files
The supplemental files for this article can be found as follows:

Text S1. Evaluation of chlorophyll-*a* concentration ocean color satellite algorithms.

Figure S1. In situ evaluation of satellite-derived chlorophyll-*a* concentration algorithms.

Text S2. Wind direction effect on chlorophyll-*a* concentration.

Text S3. Water column structure evolution in the South Hudson Bay.

Figure S2. South Hudson Bay: phytoplankton dynamic and wind components.

Figure S3. Atmosphere, ocean and phytoplankton, 2002.

Figure S4. Synergy of the sea-ice model, wind speed reanalysis, and ocean color satellites in south Hudson Bay, 2003.

Figure S5. Synergy of the sea-ice model, wind speed reanalysis, and ocean color satellites in South Hudson Bay, 2004.

Figure S6. Synergy of the sea-ice model, wind speed reanalysis, and ocean color satellites in South Hudson Bay, 2006.

Figure S7. Synergy of the sea-ice model, wind speed reanalysis, and ocean color satellites in South Hudson Bay, 2007.

Figure S8. Synergy of the sea-ice model, wind speed reanalysis, and ocean color satellites in South Hudson Bay, 2008.

Text S4. Seasonal phytoplankton photo-acclimation.

Figure S9. Seasonal influence of bio-optical properties in the Hudson Bay.

Figure S10. Seasonal influence of non-algal particles on light backscattering coefficient.

Supplementary references

Competing interests
The authors have declared that no competing interests exist. Jean-Éric Tremblay is an associate editor at *Elementa*. He was not involved in the review process of this article.

Author contributions
Conception and design: LB, SB.

Analysed, interpreted data, manuscript preparation: LB, SB, JVL, PGM.

Acquisition and processing of marine bio-optical data: LB, SB.

Sea-ice dynamic modeling: PGM.

Critical review of the manuscript: LB, SB, JVL, PGM, JET.

Final approval of the versions to be submitted: LB, SB, JVL, PGM, JET.

References
Ahmed, MMM, **Else, BGT**, **Butterworth, B**, **Capelle, DW**. 2021. Widespread surface water pCO_2 undersaturation during ice-melt season in an Arctic continental shelf (Hudson Bay, Canada). *Elementa: Science of the Anthropocene* **9**(1): 1–22.

Amante, C, **Eakins, BW**. 2009. *Etopo1 1 Arc-minute global relief model: Procedures, data sources and analysis.* Boulder, CO: National Geophysical Data Center, NOAA.

Andersson, JCM, **Pechlivanidis, IG**, **Gustafsson, D**, **Donnelly, C**, **Arheimer, B**. 2015. Key factors for improving large-scale hydrological model performance. *European Water* **49**: 77–88.

Antoine D, **Hooker, SB**, **Bélanger, S**, **Matsuoka, A**, **Babin, M**. 2013. Apparent optical properties of the Canadian Beaufort Sea—Part 1: Observational overview and water column relationships. *Biogeosciences* **10**: 4493–4509. DOI: https://dx.doi.org/10.5194/bg-10-4493-2013.

Antoine, D, Siegel, DA, Kostadinov, T, Maritorena, S, Nelson, NB, Gentili, B, Vellucci, V, Guillocheau, N. 2011. Variability in optical particle backscattering in contrasting bio-optical oceanic regimes. *Limnology and Oceanography* **56**(3): 955–973. DOI: https://dx.doi.org/10.4319/lo.2011.56.3.0955.

Ardyna, M, Babin, M, Gosselin, M, Devred, E, Belanger, S, Matsuoka, A, Tremblay, JE. 2013. Parameterization of vertical chlorophyll-*a* in the Arctic Ocean: Impact of the subsurface chlorophyll maximum on regional, seasonal, and annual primary production estimates dynamics. *Biogeosciences* **10**: 4383–4404. DOI: https://dx.doi.org/10.5194/bg-10-4383-2013.

Ardyna, M, Babin, M, Gosselin, M, Devred, E, Rainville, L, Tremblay, JE. 2014. Recent Arctic Ocean sea ice loss triggers novel fall phytoplankton blooms. *Geophysica Research Letters* **41**(17): 6207–6212.

Arrigo, KR, Van Dijken, GL. 2015. Continued increases in Arctic Ocean primary production. *Progress in Oceanography* **136**: 60–70. DOI: https://dx.doi.org/10.1016/j.pocean.2015.05.002.

Bamber, J, Van Den Broeke, M, Ettema, J, Lenaerts, J, Rignot, E. 2012. Recent large increases in freshwater fluxes from Greenland into the North Atlantic. *Geophysical Research Letters* **39**(19): 8–11. DOI: https://dx.doi.org/10.1029/2012GL052552.

Barbedo, L, Bélanger, S, Tremblay, JÉ. 2020. Climate control of sea-ice edge phytoplankton blooms in the Hudson Bay system. *Elementa: Science of the Anthropocene* **8**(1). DOI: https://dx.doi.org/10.1525/elementa.039.

Barber, DG, Hop, H, Mundy, CJ, Else, B, Dmitrenko, IA, Tremblay, JE, Ehn, JK, Assmy, P, Daase, M, Candlish, LM, Rysgaard, S. 2015. Selected physical, biological and biogeochemical implications of a rapidly changing Arctic Marginal Ice Zone. *Progress in Oceanography* **139**: 122–150. DOI: https://dx.doi.org/10.1016/j.pocean.2015.09.003.

Barbieux, M, Uitz, J, Bricaud, A, Organelli E, Poteau A, Schmechtig C, Gentili B, Obolensky G, Leymarie E, Penkerc'h C, D'Ortenzio F, Claustre H. 2018. Assessing the variability in the relationship between the particulate backscattering coefficient and the chlorophyll-*a* concentration from a Global Biogeochemical-Argo database. *Journal of Geophysical Research: Oceans* **123**(2): 1229–1250. DOI: https://dx.doi.org/10.1002/2017JC013030.

Behrenfeld, MJ. 2010. Abandoning Sverdrup's critical depth hypothesis on phytoplankton blooms. *Ecology* **91**(914): 977–989.

Behrenfeld, MJ, Boss, E, Siegel, DA, Shea, DM. 2005. Carbon-based ocean productivity and phytoplankton physiology from space. *Global Biogeochemical Cycles* **19**(1): 1–14. DOI: https://dx.doi.org/10.1029/2004GB002299.

Behrenfeld, MJ, Marañón, E, Siegel, DA, Hooker, SB. 2002. Photoacclimation and nutrient-based model of light-saturated photosynthesis for quantifying oceanic primary production. *Marine Ecology Progress Series* **228**: 103–117. DOI: https://dx.doi.org/10.3354/meps228103.

Bélanger, S, Babin, M, Tremblay, JÉ. 2013. Increasing cloudiness in Arctic damps the increase in phytoplankton primary production due to sea ice receding. *Biogeosciences* **10**(6): 4087–4101. DOI: https://dx.doi.org/10.5194/bg-10-4087-2013.

Bélanger, S, Carrascal-Leal, C, Jaegler, T, Larouche, P, Galbraith, P. 2017. Assessment of radiometric data from a buoy in the St. Lawrence estuary. *Journal of Atmospheric and Oceanic Technology* **34**(4): 877–896. DOI: https://dx.doi.org/10.1175/JTECH-D-16-0176.1.

Bellacicco, M, Cornec, M, Organelli, E, Brewin, RJ, Neukermans, G, Volpe, G, Barbieux, M, Poteau, A, Schmechtig, C, D'Ortenzio, F, Marullo, S, Claustre, H, Pitarch, J. 2019. Global variability of optical backscattering by non-algal particles from a biogeochemical-argo data set. *Geophysical Research Letters* **46**(16): 9767–9776. DOI: https://dx.doi.org/10.1029/2019GL084078.

Bellacicco, M, Pitarch, J, Organelli, E, Martinez-Vicente, V, Volpe, G, Marullo, S. 2020. Improving the retrieval of carbon-based phytoplankton biomass from satellite ocean colour observations. *Remote Sensing* **12**(21): 1–13. DOI: https://dx.doi.org/10.3390/rs12213640.

Bellacicco, M, Volpe, G, Briggs, N, Brando, V, Pitarch, J, Landolfi, A, Colella, S, Marullo, S, Santoleri, R. 2018. Global distribution of non-algal particles from ocean color data and implications for phytoplankton biomass detection. *Geophysical Research Letters* **45**(15): 7672–7682. DOI: https://dx.doi.org/10.1029/2018GL078185.

Bellacicco, M, Volpe, G, Colella, S, Pitarch, J, Santoleri, R. 2016. Influence of photoacclimation on the phytoplankton seasonal cycle in the Mediterranean Sea as seen by satellite. *Remote Sensing of Environment* **184**: 595–604. DOI: https://dx.doi.org/10.1016/j.rse.2016.08.004.

Boss, E, Pegau, WS. 2001. Relationship of light scattering at an angle in the backward direction to the backscattering coefficient. *Applied Optics* **40**(30): 5503. DOI: https://dx.doi.org/10.1364/ao.40.005503.

Brewin, RJ, Dall'Olmo, G, Sathyendranath, S, Hardman-Mountford, NJ. 2012. Particle backscattering as a function of chlorophyll and phytoplankton size structure in the open-ocean. *Optics Express* **20**(16): 17632. DOI: https://dx.doi.org/10.1364/oe.20.017632.

Brewin, RJW, Sathyendranath, S, Tilstone, G, Lange, PK, Platt, T. 2014. A multicomponent model of phytoplankton size structure. *Journal of Geophysical Research: Oceans* **119**: 3478–3496. DOI: https://dx.doi.org/10.1002/2014JC009859.

Carmack, E, Barber, D, Christensen, J, Macdonald, R, Rudels, B, Sakshaug, E. 2006. Climate variability and physical forcing of the food webs and the carbon budget on panarctic shelves. *Progress in*

Oceanography **71**(2-4): 145–181. DOI: https://dx.doi.org/10.1016/j.pocean.2006.10.005.

Carmack, E, Wassmann, P. 2006. Food webs and physical-biological coupling on pan-Arctic shelves: Unifying concepts and comprehensive perspectives. *Progress in Oceanography* **71**(2-4): 446–477. DOI: https://dx.doi.org/10.1016/j.pocean.2006.10.004.

Cleveland, WS, Grosse, E, Shyu, WM. 1992. *Statistical models in S*. Boca Raton, FL: CRC Press, Inc.

Comiso, J, Cavalieri, DJ, Parkinson, C, Gloersen, P. 1997. Passive microwave algorithms for sea ice concentration: A comparison of two techniques. *Remote Sensing of Environment* **60**(96): 357–384. DOI: https://dx.doi.org/10.1016/S0034-4257(96)00220-9.

Comiso, JC. 2000. *Bootstrap sea ice concentrations from Nimbus-7 SMMR and DMSP SSM/I-SSMIS, Version 2.* DOI: https://dx.doi.org/10.5067/J6JQLS9EJ5HU.

Cullen, JJ. 2015. Subsurface chlorophyll maximum layers: Enduring enigma or mystery solved? *Annual Review of Marine Science* **7**: 207–239. DOI: https://dx.doi.org/10.1146/annurev-marine-010213-135111.

Cushing, DH. 1990. Plankton production and year-class strength in fish populations: An update of the match/mismatch hypothesis. *Advances in Marine Biology* **26**(C): 249–293. DOI: https://dx.doi.org/10.1016/S0065-2881(08)60202-3.

Dai, A, Trenberth, KE. 2002. Estimates of freshwater discharge from continents: Latitudinal and seasonal variations. *Journal of Hydrometeorology* **3**(6): 660–687. DOI: https://dx.doi.org/10.1175/1525-7541(2002)003<0660:EOFDFC>2.0.CO;2.

de Boyer Montégut, C, Madec, G, Fischer, AS, Lazar, A, Iudicone, D. 2004. Mixed layer depth over the global ocean: An examination of profile data and a profile-based climatology. *Journal of Geophysical Research: Oceans* **109**(12): 1–20. DOI: https://dx.doi.org/10.1029/2004JC002378.

De la Guardia, LC, Garcia-Quintana, Y, Claret, M, Hu, X, Galbraith, ED, Myers, PG. 2019. Assessing the role of high-frequency winds and sea ice loss on arctic phytoplankton blooms in an ice-ocean-biogeochemical model. *Journal of Geophysical Research: Biogeosciences* **124**(9): 2728–2750. DOI: https://dx.doi.org/10.1029/2018jg004869.

Déry, SJ, Stieglitz, M, McKenna, EC, Wood, EF, Déry, SJ, Stieglitz, M, McKenna, EC, Wood, EF. 2005. Characteristics and trends of river discharge into Hudson, James, and Ungava Bays, 1964–2000. *Journal of Climate* **18**(14): 2540–2557. DOI: https://dx.doi.org/10.1175/JCLI3440.1.

Devred, E, Sathyendranath, S, Stuart, V, Maass, H, Ulloa, O, Platt, T. 2006. A two-component model of phytoplankton absorption in the open ocean: Theory and applications. *Journal of Geophysical Research: Oceans* **111**(3): 1–11. DOI: https://dx.doi.org/10.1029/2005JC002880.

Devred, E, Sathyendranath, S, Stuart, V, Platt, T. 2011. A three component classification of phytoplankton absorption spectra: Application to ocean-color data.

Remote Sensing of Environment **115**(9): 2255–2266. DOI: https://dx.doi.org/10.1016/j.rse.2011.04.025.

Doxaran, D, Leymarie, E, Nechad, B, Dogliotti, A, Ruddick, K, Gernez, P, Knaeps, E. 2016. Improved correction methods for field measurements of particulate light backscattering in turbid waters. *Optics Express* **24**(4): 3615. DOI: https://dx.doi.org/10.1364/oe.24.003615.

Dumont, D, Gratton, Y, Arbetter, TE. 2010. Modeling wind-driven circulation and landfast ice-edge processes during polynya events in northern Baffin Bay. *Journal of Physical Oceanography* **40**(6): 1356–1372. DOI: https://dx.doi.org/10.1175/2010JPO4292.1.

Eastwood, RA, Macdonald, R, Ehn, J, Heath, J, Arragutainaq, L, Myers, P, Barber, D, Kuzyk, Z. 2020. Role of river runoff and sea ice brine rejection in controlling stratification throughout winter in southeast Hudson Bay. *Estuaries and Coasts* **43**(4): 756–786.

Effler, SW, Peng, F, O'Donnell, DM, Strait, C. 2013. The backscattering coefficient and its components in the Great Lakes: A review and synthesis. *Journal of Great Lakes Research* **39**(S1): 108–122. DOI: https://dx.doi.org/10.1016/j.jglr.2013.02.002.

Enriquez, AG, Friehe, CA. 1995. Effects of wind stress and wind stress curl variability on coastal upwelling. *Journal of Physical Oceanography* **25**: 1651–1671. DOI: https://dx.doi.org/10.1175/1520-0485(1995)025<1651:EOWSAW>2.0.CO;2.

Estrada, R, Harvey, M, Gosselin, M, Starr, M, Galbraith, PS, Straneo, F. 2012. Late-summer zooplankton community structure, abundance, and distribution in the Hudson Bay system (Canada) and their relationships with environmental conditions, 2003–2006. *Progress in Oceanography* **101**(1): 121–145. DOI: https://dx.doi.org/10.1016/j.pocean.2012.02.003.

European Space Agency. 2020. *GlobColour product user guide*. ESA Data User Element Project. Available at https://globcolour.info/CDR_Docs/GlobCOLOUR_PUG.pdf.

Falkowski, PG, Oliver, MJ. 2007. Mix and match: How climate selects phytoplankton. *Nature Reviews Microbiology* **5**(12): 966. DOI: https://dx.doi.org/10.1038/nrmicro1792.

Ferland, J, Gosselin, M, Starr, M. 2011. Environmental control of summer primary production in the Hudson Bay system: The role of stratification. *Journal of Marine Systems* **88**(3): 385–400. DOI: https://dx.doi.org/10.1016/j.jmarsys.2011.03.015.

Fischer, AD, Moberg, EA, Alexander, H, Brownlee, EF, Hunter-Cevera, KR, Pitz, K, Rosengard, SZ, Sosik, H. 2014. Sixty years of Sverdrup: A retrospective of progress in the study of phytoplankton blooms. *Oceanography* **27**(1): 222–235. DOI: https://dx.doi.org/10.5670/oceanog.2014.26.

Franks, PJS. 2015. Has Sverdrup's critical depth hypothesis been tested? Mixed layers vs. turbulent layers Peter. *ICES Journal of Marine Science* **72**: 1897–1907.

Friedland, KD, Hare, JA, Wood, GB, Col, LA, Buckley, LJ, Mountain, DG, Kane, J, Brodziak, J, Lough, RG, Pilskaln, CH. 2008. Does the fall phytoplankton bloom control recruitment of Georges Bank haddock, *Melanogrammus aeglefinus*, through parental condition? *Canadian Journal of Fisheries and Aquatic Sciences* **65**(6): 1076–1086. DOI: https://dx.doi.org/10.1139/F08-040.

Fujiwara, A, Nishino, S, Matsuno, K, Onodera, J, Kawaguchi, Y, Hirawake, T, Suzuki, K, Inoue, J, Kikuchi, T. 2018. Changes in phytoplankton community structure during wind-induced fall bloom on the central Chukchi shelf. *Polar Biology* **41**(6): 1279–1295. DOI: https://dx.doi.org/10.1007/s00300-018-2284-7.

Garver, SA, Siegel, DA. 1997. Inherent optical property inversion of ocean color spectra and its biogeochemical interpretation: 1. Time series from the Sargasso Sea. *Journal of Geophysical Research* **102**(96): 18607–18625. DOI: https://dx.doi.org/10.1029/96JC03243.

Geider, RJ. 1987. Light and temperature dependence of the carbon to chlorophyll-*a* ratio in microalgae and cyanobacteria: Implications for physiology and growth of phytoplankton. *New Phytologist* **106**(1): 1–34. DOI:https://doi.org/10.1111/j.1469-8137.1987.tb04788.x.

Geider, RJ, MacIntyre, HL, Kana, TM. 1997. Dynamic model of phytoplankton growth and acclimation: Responses of the balanced growth rate and the chlorophyll-*a*: Carbon ratio to light, nutrient-limitation and temperature. *Marine Ecology Progress Series* **148**(1–3): 187–200. DOI: https://dx.doi.org/10.3354/meps148187.

Gelfan, A, Gustafsson, D, Motovilov, Y, Arheimer, B, Kalugin, A, Krylenko, I, Lavrenov, A. 2017. Climate change impact on the water regime of two great Arctic rivers: Modeling and uncertainty issues. *Climatic Change* **141**(3): 499–515. DOI: https://dx.doi.org/10.1007/s10584-016-1710-5.

Granskog, MA, Kuzyk, ZZA, Azetsu-Scott, K, Macdonald, RW. 2011. Distributions of runoff, sea-ice melt and brine using $\delta^{18}O$ and salinity data—A new view on freshwater cycling in Hudson Bay. *Journal of Marine Systems* **88**(3): 362–374. DOI: https://dx.doi.org/10.1016/j.jmarsys.2011.03.011.

Greenan, BJ, Petrie, BD, Harrison, WG, Oakey, NS. 2004. Are the spring and fall blooms on the Scotian Shelf related to short-term physical events? *Continental Shelf Research* **24**(4–5): 603–625. DOI: https://dx.doi.org/10.1016/j.csr.2003.11.006.

Halsey, KH, Jones, BM. 2015. Phytoplankton strategies for photosynthetic energy allocation. *Annual Review of Marine Science* **7**: 265–297. DOI: https://dx.doi.org/10.1146/annurev-marine-010814-015813.

Harasyn, ML, Isleifson, D, Barber, DG. 2019. The influence of surface sediment presence on observed passive microwave brightness temperatures of first-year sea ice during the summer melt period. *Canadian Journal of Remote Sensing* **45**(3–4): 333–349. DOI: https://dx.doi.org/10.1080/07038992.2019.1625759.

Harvey, M, Therriault, JC, Simard, N. 1997. Late-summer distribution of phytoplankton in relation to water mass characteristics in Hudson Bay and Hudson Strait (Canada). *Canadian Journal of Fisheries and Aquatic Sciences* **54**(8): 1937–1952. DOI: https://dx.doi.org/10.1139/cjfas-54-8-1937.

Hooker, SB, Morrow, JH, Matsuoka, A. 2013. Apparent optical properties of the Canadian Beaufort Sea—Part 2: The 1% and 1 cm perspective in deriving and validating AOP data products. *Biogeosciences* **10**(7): 4511–4527. DOI: https://dx.doi.org/10.5194/bg-10-4511-2013.

Huot, Y, Babin, M, Bruyant, F. 2013. Photosynthetic parameters in the Beaufort Sea in relation to the phytoplankton community structure. *Biogeosciences* **10**(5): 3445–3454. DOI: https://dx.doi.org/10.5194/bg-10-3445-2013.

Huot, Y, Morel, A, Twardowski, MS, Stramski, D, Reynolds, RA. 2008. Particle optical backscattering along a chlorophyll gradient in the upper layer of the eastern South Pacific Ocean. *Biogeosciences* **5**(2): 495–507. DOI: https://dx.doi.org/10.5194/bg-5-495-2008.

International Ocean Colour Coordinating Group. 2015. *Ocean colour remote sensing in Polar seas*. Dartmouth, NS, Canada: International Ocean Colour Coordinating Group. DOI: https://dx.doi.org/10.25607/OBP-107.

Jacquemot, L, Kalenitchenko, D, Matthes, LC, Vigneron, A, Mundy, CJ, Tremblay, JÉ, Lovejoy, C. 2021. Protist communities along freshwater–marine transition zones in Hudson Bay (Canada). *Elementa: Science of the Anthropocene* **9**(1): 1–20. DOI: https://dx.doi.org/10.1525/elementa.2021.00111.c.

Jakobsen, HH, Markager, S. 2016. Carbon-to-chlorophyll ratio for phytoplankton in temperate coastal waters: Seasonal patterns and relationship to nutrients. *Limnology and Oceanography* **61**(5): 1853–1868. DOI: https://dx.doi.org/10.1002/lno.10338.

Kim, Hc, Yoo, S, Oh, IS. 2007. Relationship between phytoplankton bloom and wind stress in the sub-polar frontal area of the Japan/East Sea. *Journal of Marine Systems* **67**(3–4): 205–216. DOI: https://dx.doi.org/10.1016/j.jmarsys.2006.05.016.

Koestner, D, Stramski, D, Reynolds, RA. 2020. Assessing the effects of particle size and composition on light scattering through measurements of size-fractionated seawater samples. *Limnology and Oceanography* **65**(1): 173–190. DOI: https://dx.doi.org/10.1002/lno.11259.

Kuzyk, ZZA, Macdonald, RW, Tremblay, JÉ, Stern, GA. 2010. Elemental and stable isotopic constraints on river influence and patterns of nitrogen cycling and biological productivity in Hudson Bay. *Continental Shelf Research* **30**(2): 163–176. DOI: https://dx.doi.org/10.1016/j.csr.2009.10.014.

Lannuzel, D, Tedesco, L, Van Leeuwe, M, Campbell, K, Flores, H, Delille, B, Miller, L, Stefels, J, Assmy, P,

Bowman, J, Brown, K, Castellani, G, Chierici, M, Crabeck, O, Damm, E, Else, B, Fransson, A, Fripiat, F, Geilfus, NX, Jacques, C, Jones, E, Kaartokallio, H, Kotovitch, M, Meiners, K, Moreau, S, Nomura, D, Peeken, I, Rintala, JM, Steiner, N, Tison, JL, Vancoppenolle, M, Van der Linden, F, Vichi, M, Wongpan, P. 2020. The future of Arctic sea-ice biogeochemistry and ice-associated ecosystems. *Nature Climate Change* **10**(11): 983–992. DOI: https://dx.doi.org/10.1038/s41558-020-00940-4.

Lapoussiere, A, Michel, C, Gosselin, M, Poulin, M, Martin, J, Tremblay, JE. 2013. Primary production and sinking export during fall in the Hudson Bay system, Canada. *Continental Shelf Research* **52**: 62–72. DOI: https://dx.doi.org/10.1016/j.csr.2012.10.013.

Large, WG, Yeager, SG. 2004. *Diurnal to decadal global forcing for ocean and sea-ice models: The data sets and flux climatologies.* NCAR technical notes. DOI: https://dx.doi.org/10.5065/D6KK98Q6.

Large, WG, Yeager, SG. 2009. The global climatology of an interannually varying air–Sea flux data set. *Climate Dynamics* **33**(2–3): 341–364. DOI: https://dx.doi.org/10.1007/s00382-008-0441-3.

Lee, ZP, Du, KP, Arnone, R. 2005. A model for the diffuse attenuation coefficient of downwelling irradiance. *Journal of Geophysical Research: Oceans* **110**(2): 1–10. DOI: https://dx.doi.org/10.1029/2004JC002275.

Lee, ZP, Hu, C. 2006. Global distribution of Case-1 waters: An analysis from SeaWiFS measurements. *Remote Sensing of Environment* **101**(2): 270–276. DOI: https://dx.doi.org/10.1016/j.rse.2005.11.008.

Leu, E, Søreide, JE, Hessen, DO, Falk-Petersen, S, Berge, J. 2011. Consequences of changing sea-ice cover for primary and secondary producers in the European Arctic shelf seas: Timing, quantity, and quality. *Progress in Oceanography* **90**(1–4): 18–32. DOI: https://dx.doi.org/10.1016/j.pocean.2011.02.004.

Lindström, G, Pers, C, Rosberg, J, Strömqvist, J, Arheimer, B. 2010. Development and testing of the HYPE (Hydrological Predictions for the Environment) water quality model for different spatial scales. *Hydrology Research* **41**(3–4): 295–319. DOI: https://dx.doi.org/10.2166/nh.2010.007.

Marañón, E. 2015. Cell size as a key determinant of phytoplankton metabolism and community structure. *Annual Review of Marine Science* **7**(1): 241–264. DOI: https://dx.doi.org/10.1146/annurev-marine-010814-015955.

Maritorena, S, D'Andon, OHF, Mangin, A, Siegel, DA. 2010. Merged satellite ocean color data products using a bio-optical model: Characteristics, benefits and issues. *Remote Sensing of Environment* **114**(8): 1791–1804. DOI: https://dx.doi.org/10.1016/j.rse.2010.04.002.

Maritorena, S, Siegel, DA, Peterson, AR. 2002. Optimization of a semianalytical ocean color model for global-scale applications. *Applied Optics* **41**(15): 2705–2714. DOI: https://dx.doi.org/10.1364/AO.41.002705.

Markus, T, Stroeve, JC, Miller, J. 2009. Recent changes in Arctic sea ice melt onset, freezeup, and melt season length. *Journal of Geophysical Research: Oceans* **114**(12): 1–14. DOI: https://dx.doi.org/10.1029/2009JC005436.

Matthes, LC, Ehn, JK, Dalman, LA, Babb, D, Peeken, I, Harasyn, M, Kiriliov, S, Lee, J, Bélanger, S, Tremblay, JÉ, Barber, D, Mundy, CJ. 2021. Environmental drivers of spring primary production in Hudson Bay. *Elementa: Science of the Anthropocene* **9**(1): 1–25. DOI: https://dx.doi.org/10.1525/elementa.2020.00160.

Morrow, JH, Booth, CR, Lind, RN, Hooker, SB. 2010. *Advances in measuring the Apparent Optical Properties (AOPs) of optically complex waters: The Compact-Optical Profiling System (C-OPS).* Greenbelt, MD: NASA Goddard Space Flight Center.

Mueller, JL, Fargion, GS, Mcclain, CR, Morel, A, Frouin, R, Davis, C, Arnone, R, Carder, K, Steward, RG, Hooker, S, Mobley, CD, Mclean, S, Holben, B, Pietras, C, Knobelspiesse, KD, Porter, J. 2003. *Ocean optics protocols for satellite ocean color sensor validation, revision 4.* Greenbelt, MD: NASA Goddard Space Flight Center (Radiometric measurements and data analysis protocols; vol. 3).

Mysak, L, Ingram, R, Wang, J, van der Baaren, A. 1996. The anomalous sea-ice extent in Hudson bay, Baffin bay and the Labrador sea during three simultaneous NAO and ENSO episodes. *Atmosphere-Ocean* **34**(2): 313–343. DOI: https://dx.doi.org/10.1080/07055900.1996.9649567.

Nishino, S, Kawaguchi, Y, Inoue, J, Hirawake, T, Fujiwara, A, Futsuki, R, Onodera, J, Aoyama, M. 2015. Nutrient supply and biological response to wind-induced mixing, inertial motion, internal waves, and currents in the northern Chukchi Sea. *Journal of Geophysical Research: Oceans* **120**(3): 1975–1992. DOI: https://dx.doi.org/10.1002/2014JC010407.

Olita, A, Sparnocchia, S, Cusí, S, Fazioli, L, Sorgente, R, Tintoré, J, Ribotti, A. 2014. Observations of a phytoplankton spring bloom onset triggered by a density front in NW Mediterranean. *Ocean Science* **10**(4): 657–666. DOI: https://dx.doi.org/10.5194/os-10-657-2014.

Organelli, E, Dall'Olmo, G, Brewin, RJW, Tarran, GA, Boss, E, Bricaud, A. 2018. The open-ocean missing backscattering is in the structural complexity of particles. *Nature* **9**(1): 1–11. DOI: https://dx.doi.org/10.1038/s41467-018-07814-6.

Perrette, M, Yool, A, Quartly, GD, Popova, EE. 2011. Near-ubiquity of ice-edge blooms in the Arctic. *Biogeosciences* **8**(2): 515–524. DOI: https://dx.doi.org/10.5194/bg-8-515-2011.

Platt, T, Fuentes-Yaco, C, Frank, KT. 2003. Spring algal bloom and larval fish survival. *Nature* **423**(May): 398–399. DOI: https://dx.doi.org/10.1038/423398a. Available at https://www.nature.com/articles/423398b.

Prinsenberg, SJ. 1984. Freshwater contents and heat budgets of James Bay and Hudson Bay. *Continental Shelf Research* **3**(2): 191–200. DOI: https://dx.doi.org/10.1016/0278-4343(84)90007-4.

Ras, J, **Claustre, H**, **Uitz, J**. 2008. Spatial variability of phytoplankton pigment distributions in the Subtropical South Pacific Ocean: Comparison between in situ and predicted data. *Biogeosciences* **5**(2): 353–369. DOI: https://dx.doi.org/10.5194/bg-5-353-2008.

Reda, I, **Andreas, A**. 2004. Solar position algorithm for solar radiation applications. *Solar Energy* **76**(5): 577–589. DOI: https://dx.doi.org/10.1016/j.solener.2003.12.003.

Reynolds, RA, **Stram, D**, **Mitchell, BG**, **Stramski, D**, **Mitchell, BG**. 2001. A chlorophyll-dependent semi-analytical reflectance model derived from field measurements of absorption and backscattering coefficients within the Southern Ocean. *Journal Geophysical Research: Oceans* **106**(C4): 7125–7138. DOI: https://dx.doi.org/10.1029/1999JC000311.

Reynolds, RA, **Stramski, D**. 2019. Optical characterization of marine phytoplankton assemblages within surface waters of the western Arctic Ocean. *Limnology and Oceanography* **64**(6): 2478–2496. DOI: https://dx.doi.org/10.1002/lno.11199.

Reynolds, RA, **Stramski, D**, **Neukermans, G**. 2016. Optical backscattering by particles in Arctic seawater and relationships to particle mass concentration, size distribution, and bulk composition. *Limnology and Oceanography* **61**(5): 1869–1890. DOI: https://dx.doi.org/10.1002/lno.10341.

Rho, TK, **Whitledge, TE**. 2007. Characteristics of seasonal and spatial variations of primary production over the southeastern Bering Sea shelf. *Continental Shelf Research* **27**(20): 2556–2569. DOI: https://dx.doi.org/10.1016/j.csr.2007.07.006.

Ridenour, NA, **Hu, X**, **Jafarikhasragh, S**, **Landy, JC**, **Lukovich, JV**, **Stadnyk, TA**, **Sydor, K**, **Myers, PG**, **Barber, DG**. 2019. Sensitivity of freshwater dynamics to ocean model resolution and river discharge forcing in the Hudson Bay Complex. *Journal of Marine Systems* **196**: 48–64. DOI: https://dx.doi.org/10.1016/j.jmarsys.2019.04.002.

Robinson, A, **Bouman, HA**, **Tilstone, GH**, **Sathyendranath, S**. 2018. Size class dependent relationships between temperature and phytoplankton photosynthesis-irradiance parameters in the Atlantic Ocean. *Frontiers in Marine Science* **4**(January): 1–19. DOI: https://dx.doi.org/10.3389/fmars.2017.00435.

Sathyendranath, S, **Platt, T**, **Kovač, Ž**, **Dingle, J**, **Jackson, T**, **Brewin, RJW**, **Franks, P**, **Marañón, E**, **Kulk, G**, **Bouman, HA**. 2020. Reconciling models of primary production and photoacclimation [Invited]. *Applied Optics* **59**(10): C100. DOI: https://dx.doi.org/10.1364/ao.386252.

Sathyendranath, S, **Stuart, V**, **Nair, A**, **Oka, K**, **Nakane, T**, **Bouman, H**, **Forget, MH**, **Maass, H**, **Platt, T**. 2009. Carbon-to-chlorophyll ratio and growth rate of phytoplankton in the sea. *Marine Ecology Progress Series* **383**(October): 73–84. DOI: https://dx.doi.org/10.3354/meps07998.

Sibert, V, **Zakardjian, B**, **Gosselin, M**, **Starr, M**, **Senneville, S**, **LeClainche, Y**. 2011. 3D bio-physical model of the sympagic and planktonic productions in the Hudson Bay System. *Journal of Marine Systems* **88**(3): 401–422. DOI: https://dx.doi.org/10.1016/j.jmarsys.2011.03.014.

Sibert, V, **Zakardjian, B**, **Saucier, F**, **Gosselin, M**, **Starr, M**, **Senneville, S**. 2010. Spatial and temporal variability of ice algal production in a 3D ice–ocean model of the Hudson Bay, Hudson Strait and Foxe Basin system. *Polar Research* **29**(3): 353–378. DOI: https://dx.doi.org/10.3402/polar.v29i3.6084.

Sigler, MF, **Stabeno, PJ**, **Eisner, LB**, **Napp, JM**, **Mueter, FJ**. 2014. Spring and fall phytoplankton blooms in a productive subarctic ecosystem, the eastern Bering Sea, during 1995-2011. *Deep Sea Research Part II: Topical Studies in Oceanography* **109**: 71–83. DOI: https://dx.doi.org/10.1016/j.dsr2.2013.12.007.

Smith, GC, **Roy, F**, **Mann, P**, **Dupont, F**, **Brasnett, B**, **Lemieux, JF**, **Laroche, S**, **Bélair, S**. 2014. A new atmospheric dataset for forcing ice–ocean models: Evaluation of reforecasts using the Canadian global deterministic prediction system. *Quarterly Journal of the Royal Meteorological Society* **140**(680): 881–894. DOI: https://dx.doi.org/10.1002/qj.2194.

Solonenko, MG, **Mobley, CD**. 2015. Inherent optical properties of Jerlov water types. *Applied Optics* **54**(17): 5392. DOI: https://dx.doi.org/10.1364/ao.54.005392.

Stewart, D, **Lockhart, W**. 2005. *An overview of the Hudson Bay marine ecosystem*. Winnipeg, Canada: Fisheries and Oceans Canada.

Stramska, M, **Stramski, D**, **Hapter, R**, **Kaczmarek, S**, **Stoń, J**. 2003. Bio-optical relationships and ocean color algorithms for the north polar region of the Atlantic. *Journal of Geophysical Research* **108**(C5): 3143. DOI: https://dx.doi.org/10.1029/2001JC001195.

Stramski, D, **Reynolds, RA**, **Kahru, M**, **Mitchell, BG**. 1999. Estimation of particulate organic carbon in the ocean from satellite remote sensing. *Science* **285**: 239–242.

Stroeve, JC, **Markus, T**, **Boisvert, L**, **Miller, J**, **Barrett, A**. 2014. Changes in Arctic melt season and implications for sea ice loss. *Geophysical Research Letters* **41**: 1216–1225. DOI: https://dx.doi.org/10.1002/2013GL058951.

Stroeve, JC, **Maslanik, J**, **Serreze, MC**, **Rigor, I**, **Meier, W**, **Fowler, C**. 2011. Sea ice response to an extreme negative phase of the Arctic Oscillation during winter 2009/2010. *Geophysical Research Letters* **38**(2). DOI: https://dx.doi.org/10.1029/2010GL045662.

Taylor, JR, **Ferrari, R**. 2011. Shutdown of turbulent convection as a new criterion for the onset of spring phytoplankton blooms. *Limnology and Oceanography* **56**(6): 2293–2307. DOI: https://dx.doi.org/10.4319/lo.2011.56.6.2293.

Tran, S, **Bonsang, B**, **Gros, V**, **Peeken, I**, **Sarda-Esteve, R**, **Bernhardt, A**, **Belviso, S**. 2013. A survey of carbon monoxide and non-methane hydrocarbons in the Arctic Ocean during summer 2010. *Biogeosciences* **10**(3): 1909–1935. DOI: https://dx.doi.org/10.5194/bg-10-1909-2013.

Tremblay, JE, **Lee, J**, **Gosselin, M**, **Belanger, S.** 2019. Nutrient dynamic and marine biological productivity in the greater Hudson Bay marine region, in Kuzyk, SZZ, Candlish, L, eds., *An Integrated Regional Impact Study (IRIS) ArcticNet*. Winnipeg, Canada: University of Manitoba and ArcticNet: 225–244.

Trudnowska, E, **Lacour, L**, **Ardyna, M**, **Waite, AM**, **Babin, M**, **Stemmann, L**, **Rogge, A**, **Irisson, JO**. 2021. Marine snow morphology illuminates the evolution of phytoplankton blooms and determines their subsequent vertical export. *Nature* **12**(1): 1–13. DOI: https://dx.doi.org/10.1038/s41467-021-22994-4.

Twardowski, MS, **Claustre, H**, **Freeman, SA**, **Stramski, D**, **Huot, Y**. 2007. Optical backscattering properties of the "clearest" natural waters. *Biogeosciences* **4**(6): 1041–1058. DOI: https://dx.doi.org/10.5194/bg-4-1041-2007.

Vaillancourt, RD, **Brown, CW**, **Guillard, RR**, **Balch, WM**. 2004. Light backscattering properties of marine phytoplankton: Relationships to cell size, chemical composition and taxonomy. *Journal of Plankton Research* **26**(2): 191–212. DOI: https://dx.doi.org/10.1093/plankt/fbh012.

Wang, J, **Cota, GF**, **Ruble, DA**. 2005. Absorption and backscattering in the Beaufort and Chukchi Seas. *Journal of Geophysical Research C: Oceans* **110**(4): 1–12. DOI: https://dx.doi.org/10.1029/2002JC001653.

Wassmann, P. 2011. Arctic marine ecosystems in an era of rapid climate change. *Progress in Oceanography* **90**(1–4): 1–17. DOI: https://dx.doi.org/10.1016/j.pocean.2011.02.002.

Westberry, T, **Behrenfeld, MJ**, **Siegel, DA**, **Boss, E**, **Westberry, C**. 2008. Carbon-based primary productivity modeling with vertically resolved photoacclimation. *Global Biogeochem Cycles* **22**: 2024. DOI: https://dx.doi.org/10.1029/2007GB003078.

Xi, H, **Larouche, P**, **Tang, S**, **Michel, C**. 2013. Seasonal variability of light absorption properties and water optical constituents in Hudson Bay, Canada. *Journal of Geophysical Research: Oceans* **118**(6): 3087–3102. DOI: https://dx.doi.org/10.1002/jgrc.20237.

Zhang, X, **Hu, L**, **He, MX**. 2009. Scattering by pure seawater: Effect of salinity. *Optics Express* **17**(7): 5698. DOI: https://dx.doi.org/10.1364/oe.17.005698.

Zhang, X, **Hu, L**, **Xiong, Y**, **Huot, Y**, **Gray, D**. 2020. Experimental estimates of optical backscattering associated with submicron particles in clear oceanic waters. *Geophysical Research Letters* **47**(4). DOI: https://dx.doi.org/10.1029/2020GL087100.

Zhuang, Y, **Jin, H**, **Chen, J**, **Ren, J**, **Zhang, Y**, **Lan, M**, **Zhang, T**, **He, J**, **Tian, J**. 2020. Phytoplankton community structure at subsurface chlorophyll maxima on the western arctic shelf: Patterns, causes, and ecological importance. *Journal of Geophysical Research: Biogeosciences* **125**(6): 1–15. DOI: https://dx.doi.org/10.1029/2019JG005570.

Elem Sci Anth is a peer-reviewed open access journal published by University of California Press.

OPEN ACCESS